Sindre Ertzgaard Solvang

Effect of the turbulent flow field on NOx formation in a hydrogen flame

Master's thesis in Mechanical Engineering
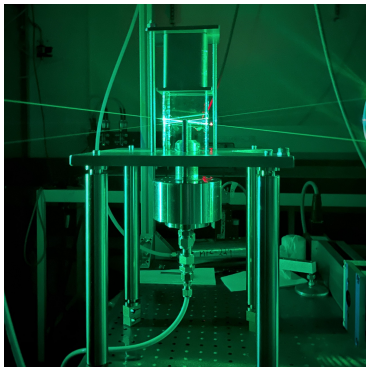Supervisor: Ivar Ståle Ertesvåg
Co-supervisor: Mario Ditaranto
June 2023

Master's thesis

NTNU
Norwegian University of Science and Technology
Faculty of Engineering
Department of Energy and Process Engineering

NTNU
Norwegian University of
Science and Technology

Sindre Ertzgaard Solvang

Effect of the turbulent flow field on NOx formation in a hydrogen flame

Master's thesis in Mechanical Engineering
Supervisor: Ivar Ståle Ertesvåg
Co-supervisor: Mario Ditaranto
June 2023

Norwegian University of Science and Technology
Faculty of Engineering
Department of Energy and Process Engineering

NTNU
Norwegian University of
Science and Technology

ABSTRACT

Given the growing urgency of climate change, the necessity to replace traditional fossil fuels has never been more critical. Gas turbines, predominantly operated using methane as fuel, contribute significantly to the carbon emissions in the oil and gas industry. This study, therefore, explored the potential of hydrogen as a substitute for methane, focusing on its impact on NOx emissions, a crucial factor for environmental considerations.

The swirling flow field above a laboratory-scale gas turbine burner was characterized using Laser Doppler Velocimetry (LDV). A recirculating zone with a height of $h = 40\,\text{mm}$, with a corresponding residence time of $\tau_{recirc} = 0.274\,\text{ms}$ was found. The flow field was found to be highly asymmetrical and complex. The mass flow rate of air corresponded to that which would result in combustion producing 10kW of power with an adiabatic flame temperature of $T_{ad} = 1563\,\text{K}$ with both methane and hydrogen as fuel.

This combustion process was simulated by constructing a Chemical Reactor Network (CRN) using Cantera that simulated the formation and consumption of NOx, in addition to the evolution of temperature in the combustion chamber. Corrected for 15% dry O_2, the model predicted NOx emissions of 21 ppm and 26 ppm with CH_4 and H_2 as fuel, respectively. When validated against experimental data, the CRN model showed high accuracy in predicting emissions when methane was used as fuel under similar conditions to the experiments. However, the model overestimated NOx emissions when hydrogen was used as fuel.

This study provides a valuable reference for future numerical models while also highlighting the feasibility of using data from cold flow measurements for accurate combustion simulation results. Furthermore, it offers preliminary insights into the potential use of H_2 as a fuel in gas turbines. The findings warrant further research on the instantaneous flow field in addition to further measurements with a combusting flow field.

SAMMENDRAG

Gitt den økende hastigheten på klimaendringene, har behovet for å erstatte tradisjonelle fossile brensler aldri vært viktigere. Gassturbiner, som hovedsakelig bruker metan som brennstoff, bidrar betydelig til karbonutslippene i olje- og gassindustrien. Derfor ble potensialet til hydrogen som en erstatning for metan undersøkt med fokus på dets innvirkning på NOx-utslipp, en avgjørende faktor for miljøhensyn.

Strømningsfeltet over en laboratorie-skala gass turbin brenner ble karakterisert ved hjelp av Laser Doppler Velocimetry (LDV). En resirkulerende sone med en høyde på $h = 40$ mm, med en tilsvarende residenstid på $\tau_{recirc} = 0.274$ ms ble funnet. Strømningsfeltet viste seg å være svært asymmetrisk og komplekst. Massestrømningsraten for luft tilsvarte det som ville produsere forbrenning som opererer ved 10 kW og en adiabatisk flammetemperatur på $T_{ad} = 1563$ K med både metan og hydrogen som drivstoff.

Denne forbrenningsprosessen ble simulert ved å konstruere et Kjemisk Reaktor Nettverk (KRN) ved hjelp av Cantera som simulerte dannelsen og forbruket av NOx, i tillegg til utviklingen av temperaturen i brennkammeret. Korrigert for 15% tørr O_2, simulerte modellen NOx-utslipp på 21 ppm og 26 ppm med CH_4 og H_2 som drivstoff, henholdsvis. Når den ble validert mot eksperimentelle data, viste KRN-modellen høy nøyaktighet i å forutsi utslipp når metan ble brukt som drivstoff under forhold like som under eksperimentene. Imidlertid overestimerte modellen NOx-utslippene når hydrogen ble brukt som drivstoff.

Denne studien gir en verdifull database for fremtidige numeriske modeller, samtidig som den understreker gjennomførbarheten av å bruke data fra kaldstrømmålinger for nøyaktige simuleringsresultater av forbrenning. Videre gir den innledende innsikt i det potensielle bruket av H_2 som drivstoff i gassturbiner. Funnene gir grunnlag for ytterligere forskning på det øyeblikkelige strømningsfeltet, i tillegg til ytterligere målinger i et strømningsfelt med forbrenning.

Contents

List of Figures

List of Tables

ABBREVIATIONS

List of all abbreviations in alphabetic order:

- **CRN** Chemical Reactor Network

- **ER** Equivalence Ratio

- **FFT** Fast Fourier Transform

- **FTIR** Fourier-Transform Infrared Spectroscopy

- **IGR** Ideal Gas Reactor

- **IRZ** Internal Recirculation Zone

- **LDV** Laser Doppler Velicometry

- **LES** Large Eddy Simulation

- **MFC** Mass Flow Controller

- **MoE** Margin of Error

- **NOx** Nitrogen Oxides

- **NTNU** Norges Teknisk-Naturvitenksapelige Universitet

- **ODE** Ordinary Differential Equation

- **ORZ** Outer Recirculation Zone

- **PIV** Particle Image Velicometry

- **PLIF** Planar Laser-Induced Fluorescence

- **PFR** Plug Flow Reactor

- **PSR** Perfectly Stirred Reactor

- **PVC** Precessing Vortex Core

- **ppm** parts per million

- **RMS** Root Mean Square

LIST OF SYMBOLS

Symbol	Description	Unit
T_{ad}	Adiabatic flame temperature	K
P	Power	W
Re	Reynolds number	-
S	Swirl number	-
$[X_F]$	Concentration fuel	$kmol/m^3$
$[X_{OX}]$	Concentration oxidizer	$kmol/m^3$
k_g	Global rate coefficient	$mol^{1n}L^{n1}s^1$
τ_c	Chemical time scale	s
δ_l	Laminar flame thickness	m
S_l	Laminar flame speed	m/s
ϕ	Equivalence ratio	-
AF_{st}	Stoichiometric air-to-fuel ratio	-
AF	Actual air-to-fuel ratio	-
$\dot{m}_{fuel}$	Mass flow rate of fuel	kg/s
$\dot{m}_{air}$	Mass flow rate of air	kg/s
J_{tg}	Tangential momentum	(kg m)/s
J_{ax}	Axial momentum	(kg m)/s
U	Mean axial velocity	m/s
W	Mean tangential velocity	m/s
$\dot{\omega}$	Net production rate of species	mol/L/s
MW	Molar weight	mol/L/s
$\dot{m}$	Mass flow rate	m/s
Y	Mass fraction	-
Q	Heat release rate	W
h	Specific enthalpy	J/kg

Symbol	Description	Unit
τ	Residence time	s
V	Reactor volume	m^3
u	Axial velocity	m/s
R_u	Universal gas constant	-
A	Cross-sectional area of plug	m^2
c_p	Specific heat capacity at constant pressure	J/(kgK)
TI	Turbulence intensity	m^3
$r_{1/2}$	Jet half width	m
S_r	Spreading rate	-
U_j	Jet velocity	m/s
S_t	Turbulent flame speed	m/s
$\bar{A}$	Time-mean of flame surface	m^2
Da_K	Small scale Damkohler number	-
Da	Large scale Damkohler number	-
E	Confidence interval	-
Z	Z-value	-

INTRODUCTION

1.1   Introduction

The urgent need to combat global warming and reduce reliance on fossil fuels has fueled a growing interest in hydrogen as an alternative energy carrier. Hydrogen is a clean energy carrier that produces no carbon emissions and can be derived from renewable power sources, making it an attractive option compared to traditional fossil fuels. Gas turbines are large emitters of carbon dioxide and could benefit from a transition to carbon-free fuels. In 2022, Norwegian Petroleum reported that gas turbines contributed to 84% of CO_2 emissions from the Norwegian oil and gas sector [1]. Using an alternative fuel source with low to no carbon emissions can lead to significant emission reductions. According to General Electric [2], natural gas-fired generation accounted for 22% of power generation globally in 2020, resulting in significant emissions worldwide that can potentially be mitigated by technological advancements. Therefore, exploring the use of hydrogen in gas turbines could provide a path to a more sustainable future. Hydrogen combustion does however face challenges. The high adiabatic flame temperature in addition to the high reactivity of hydrogen, can lead to substantial emissions of nitrogen oxides (NOx) if measures are not taken.

NOx is a term used to describe a group of compounds, including nitric oxide (NO), nitrogen dioxide (NO_2), and nitrous oxide (N_2O) that are both harmful to human health and potent greenhouse gases [3]. Concentrations of NOx can be found in the air near combustion plants or where the density of heavy combustion vehicles is high. When humans are exposed to NOx at low levels for a short amount of time, respiratory irritation can occur [4]. Prolonged exposure is linked to the development of asthma [3]. When NO_2 is introduced to the lower atmosphere, it can react with other chemicals to produce ozone, which contributes to global warming [5]. Although NO constitutes the largest portion of NOx emissions, it eventually oxidizes to NO_2 upon exposure to air. Additionally, atmospheric NOx has a high chance of forming nitric acid, which is the main constituent of acidic rain [4]. It is evident that NOx emissions must be kept as low as possible, and the Norwegian oil and gas sector has for this reason committed itself to reducing its NOx emissions by 23% from 2020 compared to emissions from 2005 [1] however, no deadline is specified.

Therefore, this study will investigate the NOx emissions from a fuel-lean fast-mixing diffusion flame, which have shown to be an effective measure for reducing the formation of NOx. However, these flames are often prone to instabilities [6]. One way of solving this is by introducing swirl to the flow, which will induce re-circulation zones that help stabilize and anchor the flame. Swirling flows involve highly complex flow phenomena, and are yet to be fully understood. The complexity makes for a hard time constructing satisfying numerical models as well, making the need for diagnostics high in order to validate potential numerical models, in addition to finding quantitative results. The intricate interplay between the flow field and chemical kinetics has been a subject of study for many years, however significant gaps in knowledge still persist.

1.2 Project Description

In response to these challenges, this thesis aims to shed light on the complexities of swirling flows and their impact on NOx emissions. The flow field above a swirl-stabilized burner will be characterized in order to model NOx emissions from a flame operated at 10 kW utilizing hydrogen and methane as fuel. Measurements of the velocity field above a swirl-stabilized burner with an isothermal flow will be conducted. The turbulent and swirling flow field will be characterized by pointwise measuring the 2D velocity components above the burner. A Laser Doppler Velocimetry (LDV) system will be used to perform the measurements.

In addition, a Chemical Reactor Network (CRN) will be developed, which will simulate NOx emissions and be validated against experimental data. Recirculation rates and residence times calculated from the experimental data will serve as input to the model, while also serving as a database to be used for future numerical models. The initial plan of the project was to make additional measurements on the reacting flow field at similar conditions and measure NOx emissions with the help of an FTIR instrument however, issues with experimental apparatus and setup caused such a delay that performing these within the time constraints was not possible. Instead, the CRN was considered a feasible replacement that could give insight into the behavior of the combustion system and predict NOx emissions.

It also made it possible to investigate the feasibility of utilizing cold flow measurement data as input into a model of a flame with a similar mass flow rate of air, pressure, and initial temperature of air. The mass flow rate used in the measurements of the cold flow field was identical to the requirements to obtain a flame with an adiabatic flame temperature of $T_{ad} = 1563$ K, and a power output of $P = 10$ kW for both methane and hydrogen and could therefore give valuable insight into how the fuels affected NOx emissions.

1.3   Previous research

In this section, a selection of the relevant literature on turbulent combustion with swirl and NOx formation will be reviewed, highlighting the key findings and gaps in knowledge that motivate the present study. Both numerical and experimental studies will be reviewed. The reviewed works will provide insight into the state of the art in turbulent combustion research and serve as a foundation for the current investigation.

1.3.1   Swirling non-reacting jets

Swirling non-reacting jets has been investigated by Lobasov et al. [7]. They utilized both PIV and PLIF techniques to examine the transfer of axial and angular momenta as well as a scalar admixture in the near-field of turbulent swirling jets (Re = 5000). The contributions from advection and turbulent diffusion were investigated, and it was found that contributions from molecular diffusion were negligible due to the turbulence in the flow. For high swirl flows, the coherent velocity fluctuations are increased by over 65 % by helical vortex structures surrounding the jet core. In contrast, for low swirl cases, the contribution was less than 22 %, which indicates that the vortex breakdown greatly enhances the mixing through turbulent transport in the near field. Increased mixing through these phenomena is of high interest in combusting cases, as it can contribute to flame stabilization and lower emissions.

The entrainment of ambient air in free-swirling isothermal air jets has previously been investigated by Cozzi et al. [8]. Various degrees of swirl were investigated from a swirl number of $S = 0$ to $S = 2.2$. The results that were obtained indicated that increased swirl will considerably improve the entrainment rate of ambient air, which can lower the formation of NOx in combustion even at low swirl levels. The onset of vortex breakdown and the presence of a Precessing Vortex Core (PVC), showed a high correlation to improving the entrainment rate. An exception was observed in the region where the swirl number was between $0.78 \leq S \leq 1.1$. In this interval, the local entrainment rate shows retardation, since the flow lies in a transition regime between the pre-and post-vortex breakdown conditions.

1.3.2   Reacting swirling jets

The turbulent flow field in a jet and its effect on the formation of NOx was per-
formed by Schmittel et al. [9]. Experiments on a 150 kW non-premixed swirl
stabilized natural gas burner was conducted, and it was found that a high swirl
number would help reduce the thermal NO formation. The study suggested that
an increased swirl intensity would lead to a higher recirculated mass flow through
the inner recirculation zone, which would lead to less thermal NO being formed.

Perhaps the most important flow field structure in swirling flows is the recircu-
lation zones. In a natural gas swirl burner, it was investigated by Coghe et al.
[10] through LDV measurements for flow field characterization, temperature mea-
surements by thin thermocouples, emission spectroscopy of the flame front, and
pollutant emissions analysis at the exhaust. The flame was confined within a
square chamber, resulting in the formation of a wide recirculation zone in the
middle of the chamber (IRZ) and large recirculating vortices in the corners of
the chamber (ORZ). Additionally, even slight enhancements in the swirl intensity
were observed to cause a notable decrease in NOx emissions. Increasing the swirl
number from 0.7 to 0.82 was found to lower NOx emissions by 30 %.

The shape of the recirculation zones exhibits minor differences between cases with
and without reactions, indicating that measurements of flow cases without reac-
tions are highly valuable according to Syred et al. [11]. This is significant, as it
indicates that calculations made for the non-reacting flow to be utilized in mod-
eling reacting flow in similar conditions. Differences can however be present as
found in a study by Dutka et al. [12]. A reacting and a non-reacting flow field
in a partially premixed bluff body burner utilizing hydrogen and methane as fuel
was investigated. For both fuels, the length of the recirculation zone increased by
1.5 when the flow field was reacting compared to the non-reacting flow field.

Three swirling CH_4 diffusion flames operated in a gas turbine model combustor and
the effects of mixing and turbulence-chemistry interactions were investigated by

Meier et al. [6] . The flames were differentiated by their power, which was operated at 7.6 kW, 10 kW, and 35 kW. Some conclusions could however be drawn for all power outputs. The study indicated that the temperature in the IRZ exhibited a higher temperature than in the ORZ, due to most gases undergoing complete reactions in this zone. In addition to this, some unburnt CH_4 was present in the ORZ, resulting in a lower flame temperature. This indicated that NOx-formation would be higher in the IRZ region of the flame.

Additionally, the flow field structures of the flames were examined [13]. Large turbulence intensities were found in the shear layer between the inlayer and IRZ, which indicates a large degree of mixing of cold and hot gases in this area. The shear layer was not indicated to be locally stable, meaning that the instantaneous flow field experiences large turbulent fluctuations. It was also found that at a power output of $P = 10$ kW, the flame experienced periodic oscillations that influenced the size of both the IRZ and ORZ.

The chemical kinetics of H_2 combustion holds significant importance in NOx formation and consumption, which has recently been investigated by Capurso et al. [14]. A swirling H_2 flame under lean conditions was examined by constructing a high fidelity compressible Large Eddy Simulation (LES) model, in addition to a new reduced mechanism for H_2/air flames which was validated against existing experimental data. As expected the thermal route proved to be dominant for NO formation. However, the NNH-route and the N_2O route was indicated to be influential in H_2 combustion as well.

The importance of the NNH-route in hydrogen flames is also supported in a numerical study by Rian et al. [15]. The importance of the mechanism is however still disputed, as noted by Glarborg et al. [16]. High-level theoretical studies on the enthalpy of formation of NNH and the reaction NNH + O, in addition to indeterminate experimental results, indicate that the importance is overstated in some modeling studies.

The choice of reaction mechanism is essential in the numerical modeling of combustion systems as it provides the foundation for constructing mathematical models, simulating chemical reactions, and predicting their behavior in complex systems.

Large efforts have therefore been made to construct both detailed and refined mechanisms. Okafor et al. [17] conducted measurements on the laminar burning velocity of CH_4/NH_3/air flames and proposed a reduced optimized reaction mechanism based on the GRI 3.0 mechanism. The GRI 3.0 was developed for natural gas flames, which means that the Okafor mechanism contains important CH_4 chemistry for combustion. The mechanism was shown to model NO concentrations well, making it a suitable choice for modeling NOx emissions from CH_4 flames.

It is evident that even though extensive research has been conducted on the interactions between the turbulent flow field and the chemical kinetics, there still exists gaps of knowledge in the field which warrants future research. Further investigation on the effects of recirculation zones on NOx formation is proposed, especially the how differences between the reacting and non-reacting flow field influences them. Further research into the role of the NNH-mechanism seems to be needed as well, as there are still disputations into its importance in NOx formation in H_2 combustion. This will help future modeling of combustion, and can contribute to realizing a shift to carbon-free fuels in future implementations in gas turbines.

1.4   Research problem specification

With this in mind, the aim of this thesis is to classify the turbulent swirling flow field above a laboratory-scale gas turbine combustor, with the aim to utilize the knowledge of the flow field to predict NOx emissions with the help of a CRN. The thesis can be condensed into three main goals:

1. Learn how to conduct 2D velocity measurements with the help of an LDV system in order to classify recirculation zones and residence times in the swirling flow field.

2. Answer if data from the non-reacting flow field can satisfactorily predict the NOx emissions from a CRN model of combustion with the same mass flow rate as air as in the conducted measurements.

3. Answer how using H_2 as a fuel influences NOx formation compared to CH_4.

1.5   Overview of the thesis

The thesis is structured in the following way:

- **Theory**: This section provides an exposition of some of the theoretical concepts of importance to the study.

- **Methodology**: This part explains in detail how LDV measurements were performed and outlines the construction of the Chemical Reaction Network (CRN) model, ensuring replicability of the study.

- **Results and Discussion**: This segment presents the main findings of the study, complemented by a comprehensive discussion. This analysis is aimed at interpreting the implications of these results in the context of current knowledge and the objectives of this study.

- **Conclusion**: The final section recapitulates the primary discoveries of the thesis, outlining their significance and potential implications for the field.

THEORY

2.1   Introduction

In this chapter an overview of some of the essential theory in the field of turbulent combustion and the formation of NOx will be presented. It is important to note that some parts of this section are based upon the project assignment [18] upon which this thesis is a continuation.

2.2   Chemical kinetics

Chemical kinetics is the branch of chemistry that investigates the speed at which chemical reactions occur and the various factors that affect their rate. Understanding chemical kinetics is crucial for comprehending the formation of important chemical species. In order to understand how the turbulent flow field influences the formation of NOx, it is essential to have a comprehensive picture of chemical kinetics.

2.2.1   Global and elementary reactions

The most common approach for describing reactions involves defining a global reaction between a moles of oxidant and 1 mole of fuel, resulting in the formation of b moles of products, expressed as $\text{F} + a\text{Ox} \longrightarrow b\text{Pr}$. This approach is often referred to as the "black box" approach since it only considers the initial reactants and the final products, without providing any insight into the complex mechanisms that occur during the reaction process.

In reality, a series of intermediate species undergo a sequence of elementary reactions to form the final product. These elementary reactions occur between the intermediate species and are critical to understanding the overall reaction process. The complete set of elementary reactions involved in the reaction process is referred to as the reaction mechanism. These mechanisms can be incredibly intricate, often involving thousands of elementary reactions [19, pp.107-109].

2.2.2   Reaction rates

For a global reaction, the reaction rate is given by the empirical equation;

$$\frac{d[X_F]}{dt} = -k_g(T)[X_F]^n[X_{OX}]^m \tag{2.1}$$

where $[X_F]$ and $[X_{OX}]$ denote the concentrations of fuel and oxidizer, respectively. k_g denotes the global rate coefficient, which is a strong function of temperature, while n and m annotate the reaction order. For a reaction mechanism with several steps, a multitude of global rate coefficients must be calculated [19, p.108].

2.2.3   Residence time

Residence time is a crucial factor that influences the formation and consumption of various species, including NOx, inside a chemical reactor. According to [20], it can be defined as the time at which a molecule enters a reactor subtracted by the time at which it leaves it. The longer the residence time, the more time reactants have to interact with each other and achieve chemical equilibrium.

Residence time can be calculated either as a time distribution or as an average for a given set of reactants. It is typically determined by dividing the volume of the reactor by the flow rate of the reactants, as explained in [21]. A precise understanding of residence time is essential for optimizing reactor design and operation, particularly in processes where NOx formation is a concern like the one in this study.

2.2.4   Chemical timescale

The chemical time scale represents the duration required for a chemical reaction to take place, serving as a valuable metric given the extensive range of reaction times that are possible. Additionally, it can provide insight into the turbulence-chemistry interactions at play, which will be discussed in a subsequent section. The determination of the chemical time scale is contingent upon the inlet conditions of the flame. For a simple, plane 1-D flame it is often determined as the ratio between the laminar flame thickness δ_l to the laminar flame speed S_l:

$$\tau_c = \frac{\delta_l}{S_l} \tag{2.2}$$

In the case of a diffusion flame matters become more complex. There is no clear definition of the laminar flame speed in this case, and therefore several chemical timescales are defined as reciprocals of the eigenvalues of the Jacobian matrix associated with the chemical source terms [22, p.151].

2.3   Equivalence ratio

The equivalence ratio (ER) contains valuable insights into the fuel-to-oxidizer concentration ratio, allowing for analysis of flame temperature, power output, and combustion product concentrations. By determining the ER, information about the formation of NOx can be gathered. Mathematically it can be expressed as:

$$\phi = \frac{(AF)_{st}}{(AF)} \tag{2.3}$$

where $(AF)_{st}$ is the air-to-fuel ratio in stoichiometric conditions, and (AF) is the actual air-to-fuel ratio [19, p.22]. Since $AF = \frac{\dot{m}_{air}}{\dot{m}_{fuel}}$, the mass flow rate of fuel can be found as:

$$\dot{m}_{fuel} = \frac{\phi \, \dot{m}_{air}}{(AF)_{st}} \tag{2.4}$$

2.4   NOx formation

In this section, the fundamental theory behind the formation and consumption of NOx will be explained. Additionally, how the quantities defined in the previous sections influence these processes will be reviewed.

2.4.1   Definition and formation mechanisms

NOx consists of the sum of NO , N_2O and NO_2 in addition to N_2O_3, N_2O_4 and N_2O_5. It is formed in most combustion processes, mainly as NO, and to a lesser extent N_2O and NO_2. Since NO and NO_2 constitute most NOx emissions, and are usually formed from anthropogenic sources, many experts refer to NOx as the sum of these compounds [23]. Formation and consumption happen in a series of competing reactions, which can be described in simplified terms as mechanisms. They can be divided into three main categories:

1. Thermal NOx formation through the Zeldovich mechanism.

2. Mechanisms that produce NO faster than predicted by the thermal mechanism. This includes the Fenimore mechanism, the NNH route, and the N_2O intermediate mechanism.

3. Fuel bound NOx formation, where N bound in the fuel is converted to NO.

The most crucial reaction routes of these mechanisms is shown in Figure 2.1.
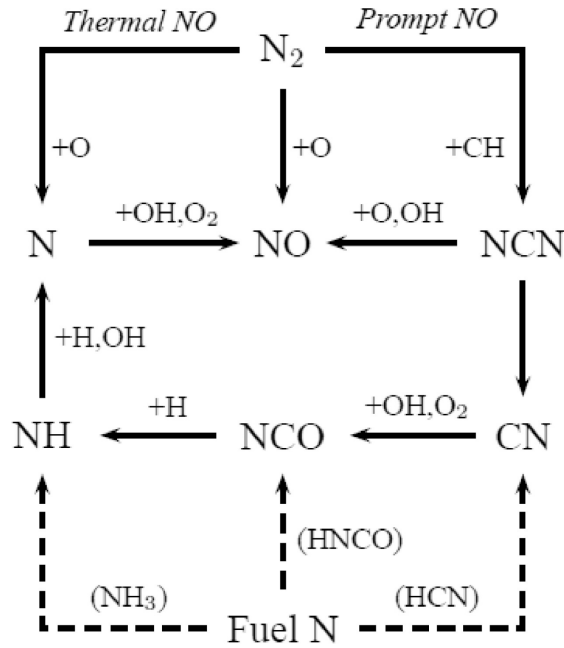
Figure 2.1: A diagram of the most important reaction routes for thermal, prompt and fuel formation of NOx. Reprinted from [16].

As H_2 does not contain any nitrogen, the thermal formation and the NNH are the main sources of formation in H_2 combustion. However, in CH_4/ air comsbustion, the Fenimore mechanism becomes important. The formation mechanisms do not exclude each other, however, different conditions can make some more prevalent than others. The conditions that are most influential on which mechanism will dominate are the concentration of radicals, equivalence ratio, temperature, residence time, and pressure. The different mechanisms and what conditions that influence them will be further explained in the following sections.

2.4.2   Zeldovich mechanism

The amount of NO formed in the Zeldovich mechanism is highly dependent on temperature and becomes evident in combustion with temperatures above 1800K [24]. NO formation by the Zeldovich mechanism is given by three chain reactions:

$$O + N_2 \rightleftharpoons NO + N \tag{2.5}$$

$$N + O_2 \rightleftharpoons NO + O \tag{2.6}$$

$$N + OH \rightleftharpoons NO \qquad\qquad (2.7)$$

Reaction 2.5 has a high activation energy of 314 kJ/mole, indicating that its temperature sensitivity.

If one assumes that the time scale is of adequate length, the concentrations of N_2, O_2, O and OH can be assumed to be at equilibrium, while N atoms can be considered at steady state. In addition to this, if one assumes that the reverse reactions involving NO can be neglected, the rate of NO concentration will be:

$$\frac{d[NO]}{dt} = 2k_{1f}[O]_{eq}[N_2]_{eq} \qquad\qquad (2.8)$$

Here, $2k_{1f}$ is the forward rate coefficient of reaction (1), and is given by [19, p.171]:

$$k_{1f} = 1.8 \cdot 10^{11} \cdot e^{-38370/T} \qquad\qquad (2.9)$$

Equation 2.8 shows that reaction 2.5 is rate limiting. The formation of NOx by the Zeldovich mechanism is influenced mainly by two factors [25]. The first is the residence time, which determines how long the time the reactions have to occur. A lower residence time will generally lead to the lower formation of NO$\cdot$ The second factor is the concentration of N_2 and O_2, which as can be seen in Equations 2.5, 2.6 and 2.7, will determine the rate of which concentration of radicals can react to form NO. In addition to this, there are indications that the air-fuel ratio is a significant factor, in the way that a decreasing air-fuel ratio leads to a reduction in NOx formation [25]. According to Glarborg et al. [16], thermal formation of NO is well understood, and the accuracy of calculations through models are limited to a greater degree by uncertainties in turbulence-chemistry interactions, than of the mechanism itself.

2.4.3 Fenimore mechanism

In turbulent diffusion flames utilizing hydrocarbons as a fuel, the Fenimore mechanism is perhaps the most important source of formation of NO [16]. It is initiated

by N_2 reacting with CH_n radicals. The reactions with NCN are of high importance for the formation of the compound, and the most important initiating reaction is indicated to be [16]:

$$CH + O_2 \rightleftharpoons NCN + H. \tag{2.10}$$

This indicates that the CH radical is the most crucial compound in the Fenimore mechanism. The barriers of triplet and singlet methylene (CH_2) are too high to contribute to the mechanism. Fuel-rich conditions are needed for it to initiate [23].

2.4.4 NNH mechanism

The routes in this mechanism are given by:

$$N_2 + H \rightleftharpoons NNH \tag{2.11}$$

$$NNH + O \rightleftharpoons NO + NH \tag{2.12}$$

The NNH mechanism is in comparison to the other mechanisms for NOx-formation and consumption, recently discovered. It has been indicated to be an important contributor to NOx formation in H_2 combustion [15][14][25]. The NNH and N_2O mechanisms are linked by the reaction between NNH and O:

$$NNH + O \rightleftharpoons N_2O + H \tag{2.9}$$

It is associated with diffusion flames, since NNH can form on the fuel-rich side of the flame sheet, which will further react with O radicals inside the flame sheet [16].

2.4.5 N_2O-intermediate mechanism

The N_2O-intermediate mechanism consists of three elementary reactions;

$$O + N_2 + M \rightleftharpoons N_2O + M \tag{2.13}$$

$$H + N_2O \rightleftharpoons NO + NH \tag{2.14}$$

$$O + N_2O \rightleftharpoons NO + NO \tag{2.15}$$

The first reaction involving three species exhibits pressure dependence. Increased pressure enhances the probability of collisions among the three species, whereas lower pressure reduces their occurrence [19, p.122]. Consequently, under high-pressure and lean conditions characterized by moderate temperatures, the reaction is commonly observed [16]. It is important to note that most formation of NO occurs either through the thermal, Fenimore, or fuel mechanisms, and formation through the N_2O- and NNH-routes are low in most combustion processes [16].

2.5   NOx control techniques

In order to control thermal NOx formation, which as explained previously is likely to be the most dominant source of emissions, the most important factors to control in combustion systems utilizing diffusion flames are:

1. Residence time

2. Temperature

3. Concentration of oxygen

Many techniques have been developed in order to achieve this, and in gas turbine applications both pre- and post-combustion control are common. Premixing and air staging are two effective control methods that are used for pre-combustion applications. The goal of both is to minimize high-temperature regions in the flow.

In air staging, the air is supplied in stages in order to change the equivalence ratio downstream in the chamber. In effect, the combustion will initiate as a rich mixture which then gets progressively leaner as air is supplied downstream. As flames have peak temperatures at stoichiometric conditions, injection of air will effectively reduce the temperature, and therefore the formation of NO through the Zeldovich mechanism [23]. This can reduce NOx-emissions with 10-40% [19, p.584]. The combustion chamber of a gas turbine can be divided into a Primary Zone (PZ), where the bulk part of the combustion takes place, and a Secondary Zone (SZ) where cold air mixes with hot products which helps cool the overall

temperature of the mixture [26]. In some gas turbine applications, it is more convenient to employ a diffusion flame rather than a premixed one, and this leads to the need for a different approach to stabilizing the flame. A common way to do this is through introducing swirl in the flow, which will be thoroughly explained in the subsequent section.

2.6 Swirling flows

Swirling flows are often used in gas turbine combustors for several reasons. It will stabilize the flame by leading hot combustion products to the root of the flame, while simultaneously improving the mixing of air and fuel. They can be investigated with laboratory swirl burners, which will be used in experiments in this thesis, and are representative of larger combustion systems. They are designed to enable data extraction and to enable visible flames [27]. The swirling flow can create an Internal Recirculation Zone (IRZ) in the inner part of the flame, in addition to an Outer Recirculation Zone (ORZ) to the right and left corners below the flame front. In the case of a non-reacting flow, the zones will usually be located in the same place however, the size of the zones may differ. The recirculation zones will improve the entrainment rate of ambient air, and can therefore help reduce the NOx emissions, as explained in Section 1.3.1.

2.6.1 Generation of swirling flows

There are three main approaches to generating a swirling flow [28]:

1. Vanes:

   By using vanes, the flow is deflected to be tangential from the axial flow. This is commonly used in gas turbines due to its simple implementation.

2. Rotating devices:

   A rotating flow will be induced by a rotating mechanical device.

3. Tangential injection:

   Fluid will be injected tangentially into the axial flow, which will cause the
   flow to swirl.

Above the swirler, a vortex forms, which will have a lower pressure in its core
compared to the ambient pressure. This creates a suction effect, drawing in am-
bient air into the vortex core. The result is the formation of recirculation zones,
as depicted in Figure 2.2. The intensity can then be controlled by adjusting the
ratio of the amount of fluid injected tangentially to the fluid flowing axially.

The tornado like nature of the central swirl-stabilized
flame is clearly evident. The flame draws gases from
downstream forming a central recirculation zone. A
side recirculation zone is also formed between the
bluff base of the combustor and the side wall.
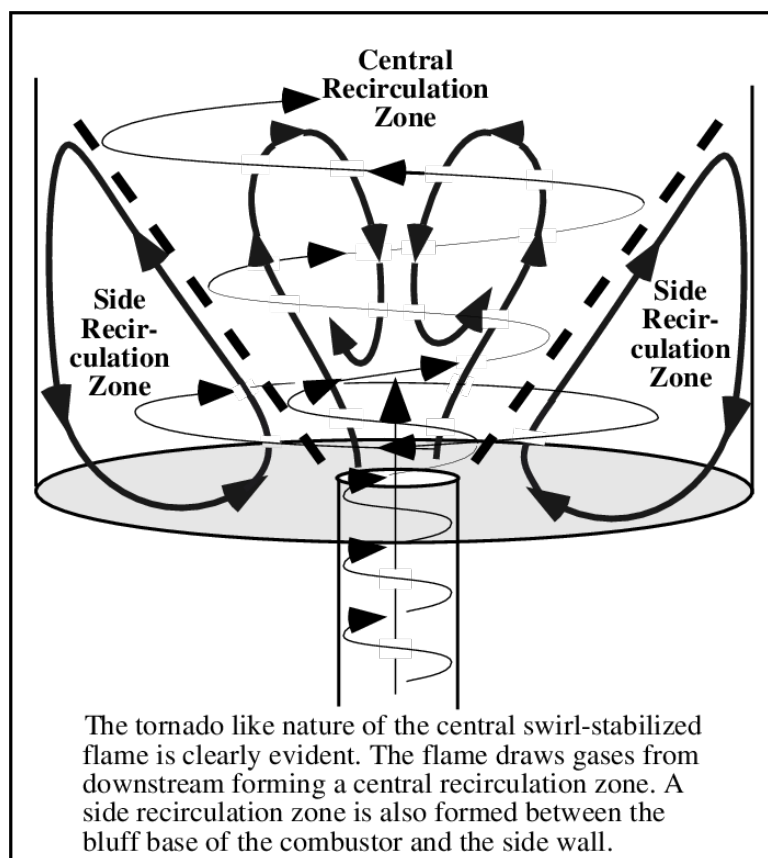
Figure 2.2: Visual representation of a swirling flow in a confined chamber. The
central recirculation zone corresponds to the IRZ, while the side recirculation zone
corresponds to the ORZ. Reprinted from [29].

2.6.2   Swirl number

A way to quantify the intensity is through the swirl number. It can be defined as
the ratio of the momentum of the tangential velocity component to the momentum

of the axial velocity component [30]. This is defined in the following equation:

$$S = \frac{J_{tg}}{J_{ax}} \tag{2.16}$$

By assuming negligible turbulent stresses compared to mean velocity terms, in addition to assuming that the boundary layer approximations are applicable, the term simplifies to [8]:

$$S = \frac{\int_0^R r^2 UW \, dr}{\int_0^R R(U^2 - 0.5W^2) \, dr}, \tag{2.17}$$

where R is the radius of the nozzle, U denotes the mean axial velocity and W denotes the mean tangential velocity. It describes the intensity of the swirl; a high swirl number indicates a high-intensity swirling flow [28]. According to Cozzi et al. [8], an increase in swirl number will improve the local entrainment rate of ambient air considerably, which will help flame stabilization and local mixing.

2.6.3 Effect of swirl on NOx-formation

An increase in swirl intensity has been shown to lead to a decrease in NOx-formation [28]. A higher swirl intensity will improve the mixing, which can lower the temperature in the IRZ, and therefore make the Zeldovich mechanism less prevalent. In addition to this, residence time in the high-temperature IRZ will be shorter with higher swirl, which will decrease NOx-formation [9]. Additionally, swirling flows often induce turbulence which will improve the mixing of reactants and products.

2.6.4 Vortex breakdown and the Precessing Vortex Core (PVC)

When the swirl intensity reaches a certain limit, vortex breakdown can occur. This is accompanied by the formation of a free stagnation point around the jet axis and the ORZ, which is located further downstream than the IRZ, in the center of the flow field. This will stabilize and anchor the flame, in addition to increasing the residence time for reactants present in the flame [8]. The precessing vortex core (PVC) is a phenomenon that can occur in combustion with swirl. This

involves the creation of a vortex core that rotates and moves circularly upstream from the flame, thereby establishing a helical vortex structure. This precessional movement is synchronized to the central cortex core. By contributing an extra heat source and prolonging the residence time of reactants within the flame, the PVC can enhance flame stability. This allows the flame to function with leaner fuel mixtures without getting extinguished [8][31].

2.7   Reactors

Coupling thermodynamic and chemical analysis can be a challenging task, which can be solved by utilizing model reactors. For the research at hand, the two most relevant are the perfectly stirred- and plug flow reactor, which will be further explained in the subsequent sections.

2.7.1   Perfectly stirred reactor

The Perfectly Stirred Reactor (PSR) is a type of 0-dimensional reactor that assumes perfect mixing within the control volume, leading to a system of nonlinear ODEs to be solved. A series of species conservation equations can be defined as [19][32]:

$$\dot{\omega}_i MW_i V + \dot{m}(Y_{i,in} - Y_{i,out}) = 0 \text{ for } i = 1, 2, ..., N \text{ species,} \qquad (2.18)$$

where:
$\dot{\omega}_i$ denotes the net production rate of species i,

MW_i denotes the molecular weight of species i,

$\dot{m}$ denote the mass flow,

$Y_{i,in}$ and $Y_{i,out}$ denote the mass fraction of species i in the inlet and outlet respectively.

This provides an equation with N equations and $N+1$ unknowns, therefore another equation is needed in order to close the problem. This is done by applying the

energy conservation equation, which takes the form:

$$Q = \dot{m} \left(\sum_{i=1}^{N} Y_{i,out} h_i(T) - \sum_{i=1}^{N} Y_{i,in} h_i(T_{in}) \right), \qquad (2.19)$$

where Q denotes the heat release rate, and $h_i(T)$ is given by:

$$h_i(T) = h_{\text{f,i}}^{\circ} + \int_{T_{ref}}^{T} c_{p,i} dT. \qquad (2.20)$$

T_{ref} is the temperature at the standard reference state, $h_{\text{f,i}}^{\circ}$ denote the enthalpy of formation, while $c_{p,i}$ is the specific heat capacity at constant pressure of species i. This model is often utilized to simulate high-velocity jets and NOx formation, making it particularly relevant to this research project [19, p.194]. The residence time is a crucial parameter in the PSR as it is the time that reactants spend in the reactor, and can have a significant impact on both the emissions and performance of the combustion chamber. It can be found in a PSR as [19, p.196]:

$$\tau = \frac{\rho V}{\dot{m}} \qquad (2.21)$$

2.7.2 Plug flow reactor

A Plug Flow Reactor (PFR) is a type of 1-dimensional reactor where fluid mixing is assumed to occur only radially, but not axially. PFRs are usually modeled as cylindrical in shape, operating under steady-state flow conditions and ideal gas conditions, with negligible viscous effects [19, p.206]. These reactors are typically employed to simulate combustion processes with low degrees of mixing, which frequently occur towards the end of the combustion chamber, where fuel consumption is high, and turbulence intensity is low [32]. The governing equations that need to be integrated in a PFR are [19, pp. 209-210]:

$$\frac{d\rho}{dx} = \frac{\left(1 - \frac{R_u}{c_p MW_{mix}}\right) \rho^2 u^2 (\frac{1}{A}) \frac{dA}{dx} + \frac{\rho R_u}{u c_p MW_{mix}} \sum_{i=1}^{N} MW_i \dot{\omega}_i \left(h_i - \frac{MW_{mix}}{MW_i} c_p T\right)}{P\left(1 + \frac{u^2}{c_p T}\right) - \rho u^2}$$

$$(2.22)$$

$$\frac{dT}{dx} = \frac{u^2}{\rho c_p} \frac{d\rho}{dx} + \frac{u^2}{c_p} \left(\frac{1}{A} \frac{dA}{dx}\right) - \frac{1}{u \rho c_p} \sum_{i=1}^{N} h_i \dot{\omega}_i MW_i \qquad (2.23)$$

$$\frac{dY_i}{dx} = \frac{\dot{\omega}_i MW_i}{\rho u},$$
(2.24)

where:

u is the axial velocity,

R_u is the universal gas constant,

A is the cross-sectional area of the plug.

Within the PSR, a residence time can be defined as:

$$\frac{d\tau}{dx} = \frac{1}{u}$$
(2.25)

In order to solve the equations the initial conditions needed are: $T(0) = T_0$, $\rho(0) = \rho_0$, $Y_i(0) = Y_{i0}$ for $i = 1, 2..., N$, and $t_r(0) = 0$. Similar to the PSR model, the residence time is a crucial parameter in the PFR. However, since the residence time in a PFR is a function of the flow rate and its dimension, it is not constant and can be difficult to estimate [19, p.209].

2.7.3   Chemical Reactor Networks

A Chemical Reactor Network (CRN) is a way to model finite-rate combustion. The working principle is to divide the flame into smaller regions where variations in chemical properties are low. This allows for the regions to be modeled by reactors such as PFRs and PSRs. A region can be modeled by one reactor, or in some cases such as recirculation zones, several. The reactors upstream are connected with inlet conditions from preceding reactors. While a CRN excels in accurately representing the chemistry involved, it has limitations in capturing the intricate effects of the flow field to a significant extent [32].

2.8   Turbulence

Turbulence is an irregular motion of a fluid, brought on by various forces such as pressure gradients that can lead to flow separation, or shear forces causing vortices. This type of movement is useful in combustion processes as it helps to enhance

the mixing of fluids, leading to improved combustion efficiency. Additionally, turbulence can offer a number of other benefits such as increased energy transfer and improved heat removal.

2.8.1 Mean flow, turbulence intensity, RMS

As turbulence is a complex and unpredictable phenomenon, qualitative descriptions alone are often insufficient. Therefore, a statistical approach is necessary to quantitatively characterize turbulence. The time mean of velocity is a statistical quantity that represents the average velocity over a certain time period at a given location in a turbulent flow. By averaging the velocity data over time, the time mean can help identify trends and patterns in the flow, providing insights into the overall behavior of the turbulent flow.

The time mean of velocity is particularly useful because it can be measured experimentally or computed from numerical simulations. It serves as a reference value against which turbulent fluctuations can be compared. Deviations from the time mean of velocity provide information about the strength and direction of the turbulent fluctuations.

Commonly, the velocity is decomposed when dealing with problems within the turbulent flow, called Reynolds decomposition. The velocity, $U(x,t)$, is composed into its fluctuations and its mean flow [33, p. 83];

$$U(x,t) = \bar{U}(x,t) + u(x,t) \tag{2.26}$$

Where $\bar{U}(x,t)$ is the time mean of the flow and $u(x,t)$ are the velocity fluctuations. By taking the root mean square of the velocity, $u_{rms}(x,t)$, it is possible to gain insight into the level of turbulence as it gives an indication of the magnitude of the velocity fluctuations. From these quantities, the turbulence intensity can be defined as [34]:

$$TI = \frac{u_{rms}(x,t)}{\bar{U}(x,t)} \tag{2.27}$$

2.8.2   The turbulent energy cascade

Turbulent flows consist of eddies, a whirling motion of the fluid caused by velocity fluctuations. As the size range of eddies within a flow can differ by several orders of magnitude, they have characteristic scales defined, governed by their size. Each eddy has an intrinsic length scale, L, velocity scale, $u(l)$, and time scale $\tau(l) = \frac{l}{u(l)}$. Kinetic energy is introduced to the flow at the largest motion scales and is then transferred to smaller and smaller scales through inviscid action, until it is dissipated through viscosity, mainly at the smallest scales. The reason for the breakdown of the largest eddies is their inherent instability. As the eddies diminish in size, the Reynolds number drops to a point where the effect of viscosity becomes significant. At this point, viscous action dominates and converts the kinetic energy of the fluid motion into heat energy [33, p. 183].

2.8.3   Kolmogorov hypotheses

From 1941-1942 Kolmogorov proposed three hypotheses that are still fundamental to this day in turbulence theory. The first theory regards the local isotropy of small-scale motions. He proposed that when the Reynolds number is sufficiently high, the small-scale turbulent motions exhibit statistical isotropy. This suggests that changes in the direction of small eddies are uncorrelated with those of large eddies and are equally likely to occur in any direction, regardless of the mean flow. According to Kolmogorov, eddies smaller than a certain length scale, denoted as l_{EI}, belong to the universal equilibrium range, which is typically set to approximately $\frac{1}{6}$ of the large length scale l.

This is due to small-scale eddies rapidly reacting to changes from the large scales and the mean flow and is therefore in approximate equilibrium. In the universal equilibrium range, the statistics are only dependent on viscous forces and the transfer of kinetic energy from larger scales. In addition, kinetic energy transferred from larger eddies is assumed to be equal to the dissipation rate [35, p. 127],[33, p. 184]. Moreover, Kolmogorov suggested that eddies of a specific size should be categorized into an inertial subrange ($l_{DI} < l < l_{EI}$), where inertial effects dominate, and a dissipative range ($l < l_{DI}$), where viscous effects play a crucial role.

The length scale l_{DI} acts as a boundary, dividing the universal equilibrium scale into the dissipative and inertial subranges, and resides between the two.

The regions can be defined with respect to how the turbulent kinetic energy develops as a function of the wavelength number. The wavelength κ is inversely proportional to the characteristic length scale of the eddies, hence as the wavelength increases in value, the eddies reduce in size. As shown in Figure2.3 the eddies containing the most energy are of larger size which is defined as being in the inertial region, while smaller eddies that contain less energy are defined as being in the dissipative region [35, pp. 128-130].
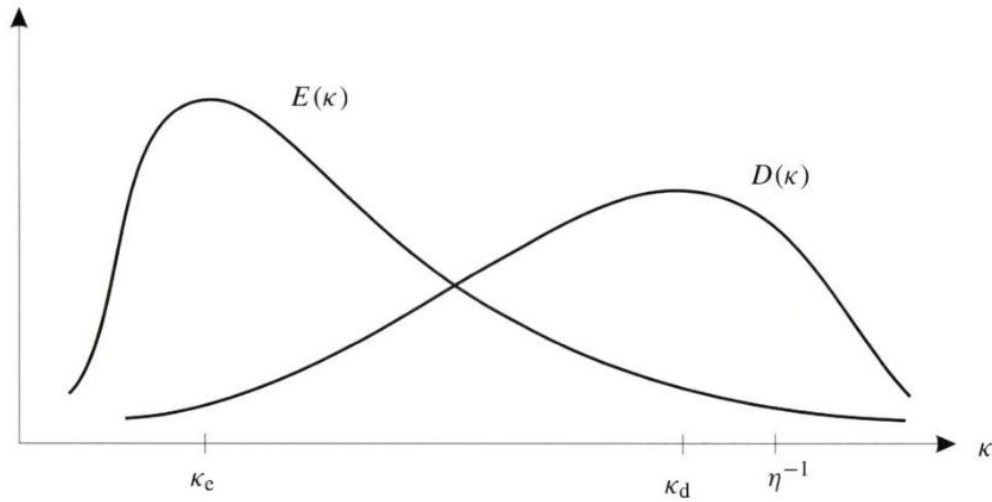
Figure 2.3: The turbulent energy spectrum is represented graphically, with the wavenumber plotted along the x-axis, while the energy spectrum and dissipation spectrum are plotted along the y-axis. Reprinted from [35, p. 125]

2.8.4 Turbulent time scales

Inherent to the eddies exists a turbulent time scale as well as a length scale. The turbulent time scale represents the rate at which energy is transferred between turbulent eddies and can be used to estimate how long it will take for the energy contained in larger eddies to be dissipated into smaller scales. For the large scales, it is defined as θ, while it is defined as τ for the small scales. θ can be estimated as the ratio of the characteristic length scale to the characteristic turbulent velocity scale :

$$\theta = \frac{l}{U} \tag{2.28}$$

At the small scales, also called the Kolmogorov scales, the time scale can be defined as:

$$\tau = \left(\frac{\nu}{\epsilon}\right)^{\frac{1}{2}} \tag{2.29}$$

Where ν is the viscosity, and ϵ is the turbulent dissipation rate [33, p.184]. They can be used to define different flame regimes with the help of a chemical time scale, which will be further explained in the following section.

2.8.5 The turbulent jet

In order to understand the flow phenomena present in this study, a description of the round turbulent jet is useful. As described by Pope [33, pp.96-102], the jet is assumed to be axisymmetric and ejected into a quiescent fluid. The flow is steady from the nozzle, producing a flat-topped axial velocity profile. Importantly, the flow is independent of the axial and radial coordinates, and is ideally perfectly described by the jet velocity U_J, the nozzle diameter d and the kinematic viscosity ν.

The mean axial velocity is one order of magnitude larger than the radial velocity and is therefore the main interest when discussing the turbulent jet. One important characteristic of the radial velocity is that it becomes negative at the edges of the jet, indicating the entrainment of the surrounding fluid. This feature holds significant relevance in cases involving reacting flows.

However, perhaps the most important feature of the jet is that it is self-similar. This means that the velocity profiles of different axial positions can be collapsed on a single curve by scaling the velocities with correct scaling factors. It makes for easier and more efficient modelling of the jet. Another important feature is the spreading rate S_r, which describes the rate at which the jet spreads from its origin. It is found to have a linear behaviour.

The linear behaviour allows for the jet half-width $r_{1/2}(x)$, which is the radial distance from the centerline of the jet to the point it reaches $\frac{1}{2}U_0(x)$, to be defined as:

$$r_{1/2}(x) = S_r(x - x_0) \tag{2.30}$$

Furthermore, self-similarity makes it so that the centerline velocity, $U_0(x)$ can be described in linear terms as:

$$\frac{U_0(x)}{U_J} = \frac{B}{(x - x_0)/d} \tag{2.31}$$

where B is an empirical constant, and x_0 is the virtual origin, at which the mean axial velocity is zero.

This leads to the important conclusion that the local Reynolds number:

$$Re = \frac{U_0 \, r_{1/2}}{\nu} \tag{2.32}$$

is independent of x, as $U_0(x)$ scales linearly with x^{-1} and $r_{1/2}(x)$ scales linearly with x.

2.9 Turbulent flames

Due to the highly complex nature of turbulence and combustion, this is an area of study that still relies heavily on empirical observations. Characteristic scales developed for laminar flames have proved to be useful when performing calculations for turbulent flames. Two important quantities are the laminar flame speed u_L and the flame thickness δ_L. These laminar scales can be used since they are defined from the reaction rate, and not from properties of the flow [35, p. 152].

2.9.1 Flame speed

The laminar flame speed can be defined as the propagation rate of the flame front relative to the unburnt mixture. It can influence the efficiency of the combustion, as well as emissions. For premixed flames, it holds information on diffusivity, reactivity and the heat released from the reactions taking place [36]. For a turbulent flow the turbulent flame speed, S_t, depends on not only the thermal and chemical properties of the mixture but also the nature of the flow field and its interaction with the chemistry. It can be defined as the velocity of the unburnt mixture as it enters the reaction zone of the flame in a normal direction to the flame. Due to

the fluctuating nature of the turbulent flow, the flame area is a mean-time value. This can be expressed mathematically as:

$$S_t = \frac{\dot{m}}{\overline{A}\rho_u},$$

(2.33)

where $\dot{m}$ represents the reactant flow rate, $\overline{A}$ is the time-mean of the flame surface, and ρ_u the density of the unburnt gas [19, p. 457] .

2.9.2   Flame thickness

The unstretched laminar flame thickness can be defined as the ratio of the temperature difference between the burnt and unburnt gas to the maximum spatial temperature gradient which can be seen in Figure 2.4. The flame thickness can be used in modelling as well as quantifying combustion regimes [37].
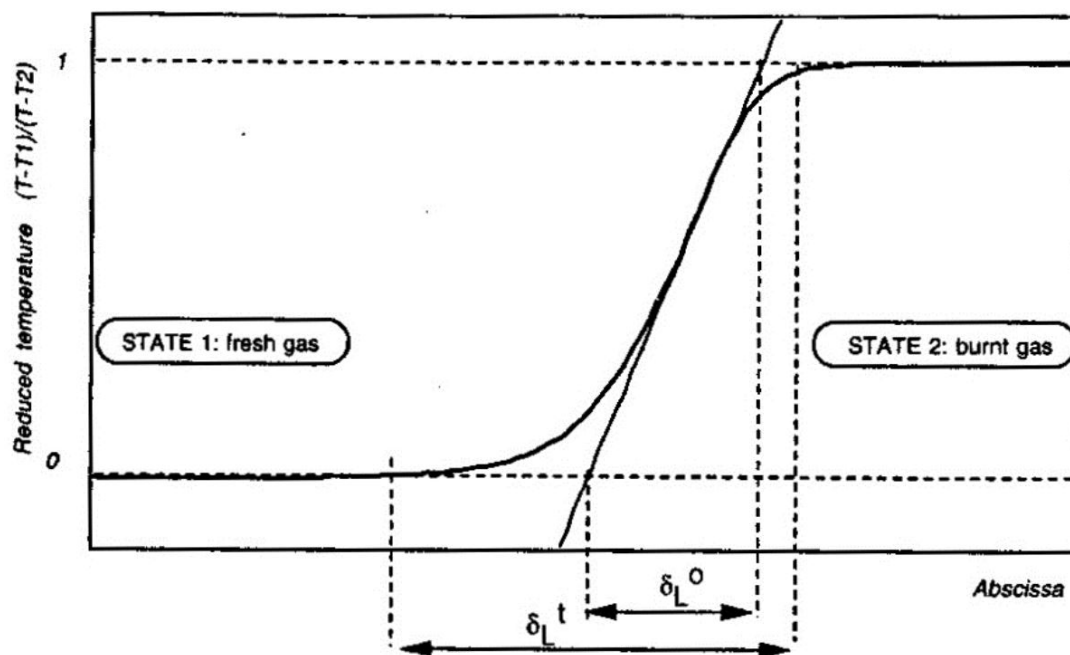

Figure 2.4: Illustration of the flame thickness. δ denote the stretched flame thickness, while δ° denote the unstretched flame thickness. Reprinted from [38]

2.9.3   Damköhler number

A useful parameter when performing engineering calculations on turbulent flames is the Damköhler number, defined as the ratio of the characteristic turbulent time

scale to the characteristic chemical time scale [19, p. 461]. There is one Damköhler number for the small scales [35, p. 152] ;

$$Da_K = \frac{\tau}{\tau_c} \tag{2.34}$$

In addition to this there is one Damköhler number for the large structures;

$$Da = \frac{\theta}{\tau_c} \tag{2.35}$$

The inverse of this number is frequently used and is then referred to as the Karlovitz number Ka. The interactions between turbulence and chemistry can be quantified by this number, which can be used to classify different combustion regimes. For $Da \gg 1$ the turbulence will be intense, while the reactions are slow. The flame will be distributed over a large area, which can occur in industrial furnaces. For $Da \ll 1$, the reaction rate is controlled by the chemistry at hand. For these types of flames, the turbulence is weak. The combustion takes place in laminar sheets, that can be distorted into wrinkled flames, depending on the strength of the turbulence. If both turbulence and chemistry are of equal importance, the Damköhler number approaches unity.

The different combustion regimes can be further investigated in a Borghi diagram. It is a logarithmic plot that shows the relation between the burning velocity and the flame thickness. Turbulent fluctuations will cause the reaction zone to be distorted, and large fluctuations will cause these distortions to separate and form pockets. Pockets can also form containing only reactants or only products. As explained earlier it is also possible for the reaction zone to be spread out over a large area in the case of slow reaction rates. All of these different regimes are captured in a Borghi diagram, which can be seen in Figure 2.5. The lower left corner under the line indicating $Re_t = 1$ corresponds to a laminar regime [39].
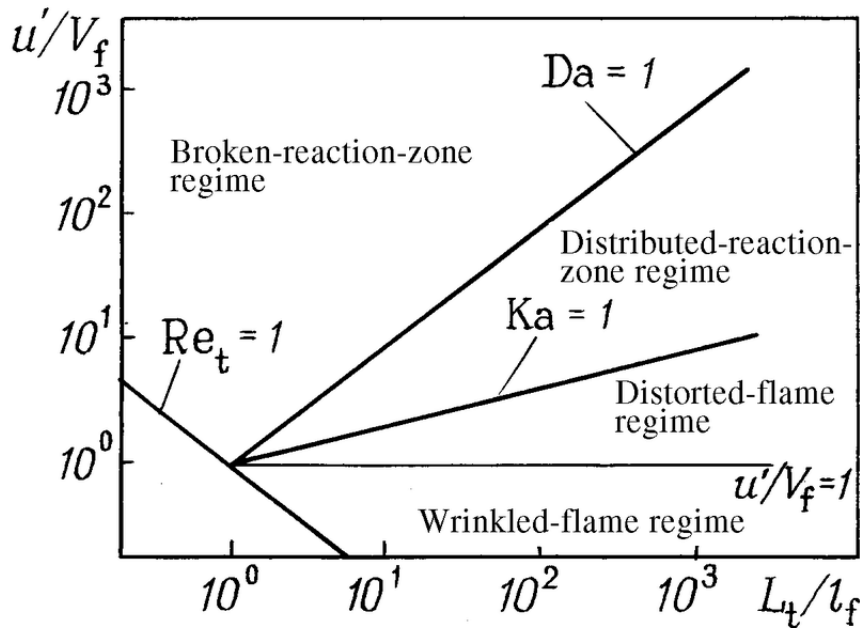
Figure 2.5: Borghi diagram. V_f is the flame speed, L_t is the turbulent length scale and l_f the flame thickness in this notation. Da corresponds to Da_k. Note that the absolute values on the x- and y-axis is not accurate for the case in this study. Reprinted from [40].

2.10   Diffusion and premixed flames

If fuel and oxidizer are mixed before the ignition of a flame occurs, the conditions are met for a premixed flame. Combustion more often reaches completion in this type of flame compared to a diffusion flame and is often used to lower the combustion temperature and therefore emissions of NOx. The reactions often propagate as multiple laminar flame sheets that can be more or less distorted depending on the strength of the turbulent fluctuations [41]. On the other hand, in a diffusion flame, fuel and oxidizer are mixed together through molecular diffusion and convection. This can be a slow mixing process, however, by introducing turbulence in the flow field of the flame, the mixing process will be greatly enhanced compared to laminar flames. They can however be extremely complex, due to the turbulence-chemistry interactions. The flame can be spread across a wide range of Damköhler numbers, and be in a non-equilibrium state [42]. To gain a new understanding of these complicated processes are of high interest, and is one of the motivations for this study.

THREE

METHODS

3.1 Introduction

A quantitative experimental study was conducted to investigate the non-reacting turbulent swirling flow field from a model gas turbine burner. The 2D velocity field was characterized with a Laser Doppler Velocimeter (LDV) system, and calculations were conducted on the residence times and recirculation rates. These values served as input into a Chemical Reaction Network in order to simulate NOx emissions from the corresponding reacting flow field. The following chapter will explain how the CRN was constructed and how data from the LDV was obtained, in addition to its operating principles.

3.2 Facility

The experiments were carried out at Varmetekniske laboratorier at NTNU. A square combustion chamber with a height of 18 cm, a width and length of 6.7 cm was placed above the burner, as seen in Figure 3.1. The bottom part of the chamber, where the measurements were made, was made of fused quartz due to its excellent thermal properties, as well as optical transparency. It has a low linear

thermal expansion coefficient of $\alpha = 5.5 \cdot 10^{-7}$ m/(mC), which makes it suitable to withstand the high temperatures of H_2 combustion [43]. A Lexel 95 Argon ion laser was utilized. 4 continuous laser beams of maximum intensity of 250 mW each were emitted from the laser head. At the focal length of 310 mm away from the focusing lens, the beams were focused in order to obtain an intensity maximum of 1 W, which is where the measurements were conducted. The transverse beams had a wavelength of 488 nm, while the longitudinal beams had a wavelength of 514.5 nm. The scattered light was received by a photomultiplier which converted the Doppler-shifted light to an electrical signal. The experimental setup can be seen in Figure 3.2.
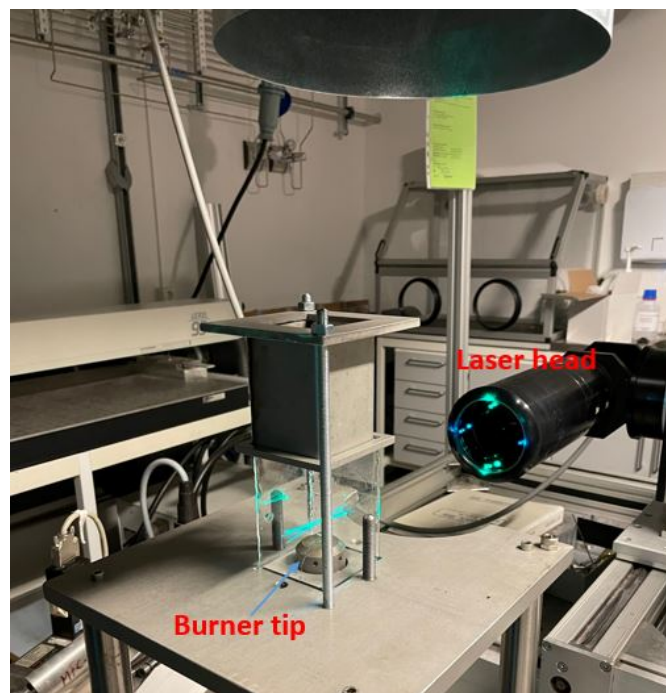
Figure 3.1: View of the combustion chamber. The bottom is made of fused quartz, while the chimney is made of stainless steel.
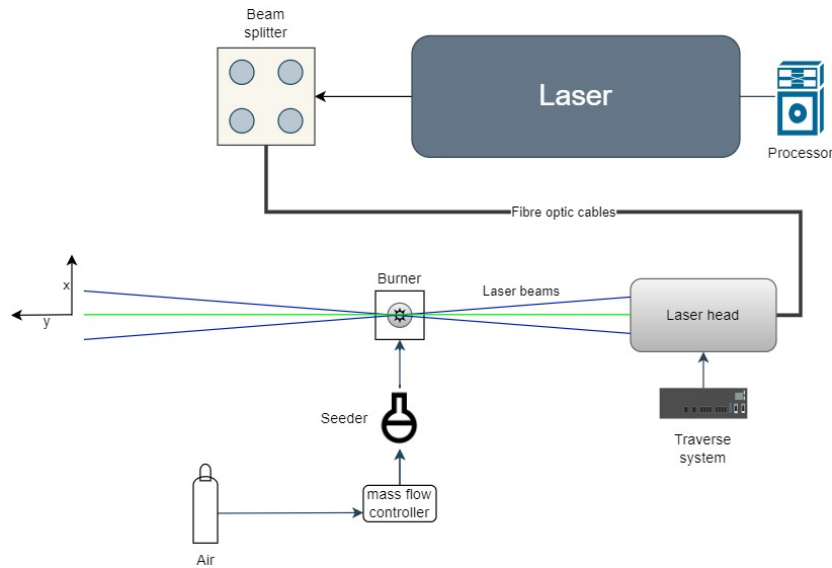
Figure 3.2: Experimental setup as viewed from above. The laser beam is sent to a beam splitter, which is transmitted to a laser head that converges the four beams on the measuring volume straight above the burner. The traverse system enables and controls the motion of the laser head.

3.3 Burner

The burner used in this study is a modified version of the Siemens Energy SGT-A35 conventional Dual-Fuel burner and is shown in Figure 3.3. It is modified to still have the same combustion characteristics as the combustion system in the gas turbine [44] It has a burner tip diameter of 40 mm, and the total length of the burner is 145 mm. The airflow is directed into a primary channel and subsequently divided into two separate paths. 31.25% of the air is guided to the swirler, which guides the air through angled vanes, while the remaining air is channeled through six smaller channels that emit the air in a radial pattern. The combined effect of the air ejection from the main air holes, and the swirler section induce swirl to the flow field. The main air holes have a diameter of 3 mm, while the fuel is ejected through 6 holes with a diameter of 1.1 mm placed above the main air holes. Fuel is fed through a separate channel in order to obtain a diffusion flame. The air inlet has a diameter of 16 mm, while the fuel inlet has a diameter of 12 mm. In the burner assembly, only two out of the six main air inlets were aligned parallel to each other, while the remaining were not. This resulted in an asymmetric configuration with significant implications for the characteristics of the flow field.
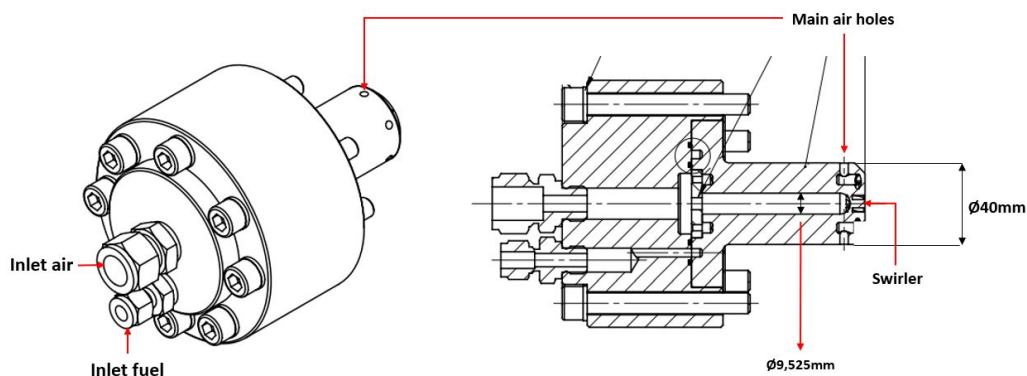
Figure 3.3: Schematic showing the external and internal geometry of the burner. Figure adapted from an original machine drawing provided by Tresh + Kiegler Engineering.

3.4   Laser Doppler Velocimetry

LDV is a non-intrusive measurement technique that captures fluid dynamic effects in the flow field without disrupting it. It provides high precision, in addition to high temporal and spatial resolution. The directional sensitivity of the LDV makes it ideal for measuring recirculating flows. [45]. The operating principles of the LDV measuring technique used in the study will be explained in the following section.

3.4.1   Doppler shift

The operating principle of an LDV is rooted in the Doppler shift of light that has been refracted or reflected by seeding particles. The laser beam is targeted toward these tiny particles, typically on the micrometer scale, which serve as seed particles. The incoming light has a given frequency, however, when this is scattered the seeding particle observes a different frequency due to the particle movement. In order to measure the frequency shift, the light scattered from two intersecting beams is mixed. Due to the different angles of the laser beams, they will have different frequencies. When combined, they create a Doppler frequency caused by constructive and destructive wave patterns. This frequency is proportional to the

velocity of a particle, enabling velocity measurement.

3.4.2   Bragg cell

One potential issue that may arise is the inability of the receiver to distinguish be-
tween positive and negative frequencies, leading to a lack of differentiation between
positive and negative velocities. However, this challenge is effectively addressed
by incorporating a Bragg cell into the system. A 40 MHz Bragg cell is positioned
in the path of one of the beams before reaching the beam splitter and is capable
of inducing a frequency shift in the diffracted beam. This frequency shift ensures
that there is no ambiguity in the direction of the velocity being measured [46].

3.4.3   Backward scatter

Because of the dimensions of the seed particles, a majority of the signal is dispersed
away from the transmitter. As a result, many LDV methods use a receiver located
upstream of the transmitter, a technique referred to as forward scatter LDV.
However, some of the scattered light is redirected back to the transmitters optics,
where a receiver can detect the velocity of the particles through a photomultiplier.
This is known as backscatter LDV and will be utilized in this study [46]. It will
minimize the need for alignation between the parts, and therefore save time. The
most important principles are illustrated in Figure 3.4.

3.4.4   Seeding particles

One of the most important choices that have to be made to make high quality
data acquisition is what type of seeding particle to use. The seeding particle con-
veys the velocity of the flow, and it is therefore necessary that it is a good light
scatterer, in addition to being chemically inert. It should be small enough to be
able to follow the flow accurately but, at the same time be large enough to scatter
the light in a satisfactory manner. When choosing particles shape and size are
crucial considerations. The shape of the particles affects the drag forces that act
upon them, while size determines how light is scattered. Large particles will pri-
marily reflect light from their surfaces, whereas for smaller particles, diffraction,

and polarization of incident light are important factors [46].

Silicone oil particles were chosen for the experiments, as they are well suited for use in airflows. Polydimethylsiloxane was chosen as the source of seeding particles for the experiments. This is a silicone oil, which is very satisfactory in use with air flows [46]. The liquid silicone oil was placed in a container underneath the burner, where it was seeded into the airflow through a bypass system as illustrated in Figure 3.5. In the system air is injected into a container containing the seeding oil at high speeds, creating a low-pressure zone at the top of the container. The resulting suction draws seeding particles up from the bottom of the container where it mixes with the airflow. A throttle valve is used to control the mass flow rate of the main air, while a second valve is used to control the seeding particle rate.
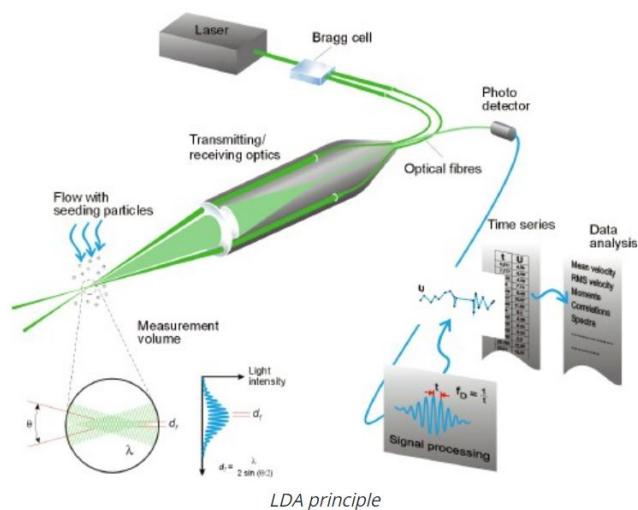
Figure 3.4: Illustration of the fundamental principles in a backscatter LDV system from Dantec Dynamics [45].
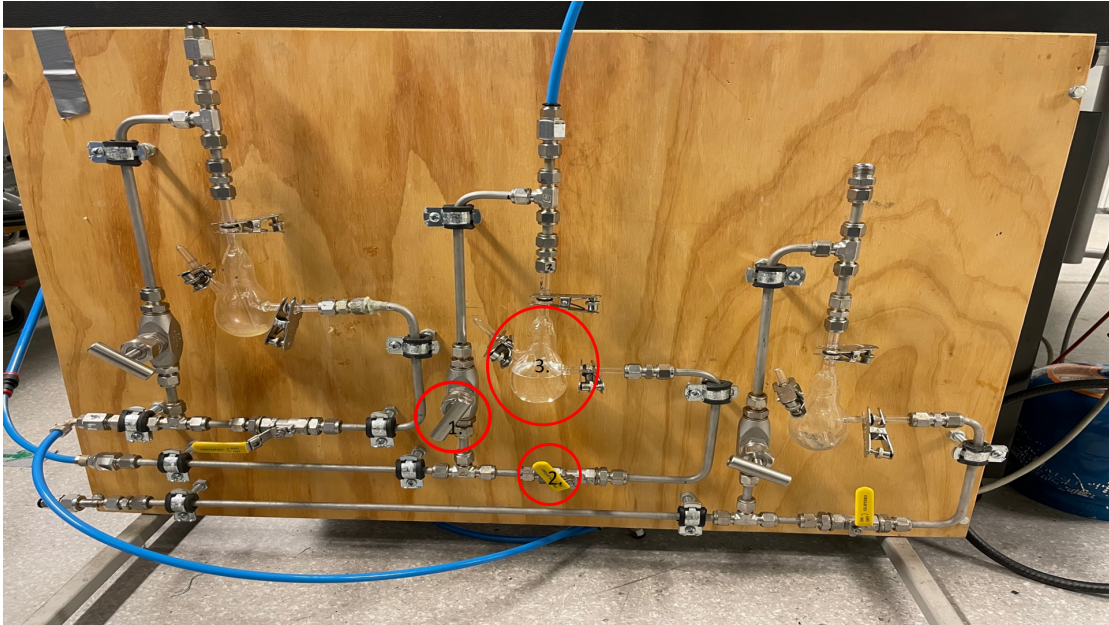
Figure 3.5: A picture of the seeding bypass system. (1.) depicts the throttle valve, (2.) the valve, and (3.) the seeding oil container.

3.5   Experiments

3.5.1   Method

In order to characterize the flow, measurements were conducted at different regions of interest using LDV. The position of the laser head, and thus the focal point of the measurements, was adjusted by a computer-aided linear traverse controller from Dantec Dynamics, enabling measurements of the 2D flow field. The mass flow rate of the pressurized air was controlled by a Brooks 0154 Mass Flow Controller to maintain the desired mass flow rate from the burner with an associated uncertainty of 0.1 % of the maximum input/output range [47]. It was adjusted to achieve a mass flow rate of 4.6 g/s, which is the required flow rate for generating a flame with $T_{ad} = 1563$ K, and a power output of 10 kW with both hydrogen and methane as fuel. The air was guided through the bypass system which allowed for the control of the amount of seeding particles passing through the flow, and thus the data rate.

3.5.2   Data acquisition and analysis

The output of the velocity measurement was a current pulse, which conveys information about the velocity as well as any background noise present. To obtain high-quality data, it was crucial to select the optimal bandwidth that corresponds to the velocity range, in order to minimize noise in the signal. If the velocity range is small, a narrow bandwidth was required, whereas, for large velocity ranges, a broader bandwidth was necessary. Additionally, the number of seed particles in the measurement volume was another crucial factor. Ideally, only one particle should be present in the volume at any given time for the most accurate results [46].

Other factors which impact the data rate and in turn, the validity of the data was the sensitivity chosen on the photomultiplier, and the signal gain chosen on the photo-multiplier signal amplifier. The measurements were taken in coincidence mode, which ensured that if two or more particles were to have the same arrival time in the measuring volume, calculations were only performed on one velocity component. As the direction of velocity in a jet is primarily in the axial direction, velocity bias should be unlikely to occur due to this. The data was acquired by the BSA Flow Software v4.1, through the BSA-F60 Flow Processor.

When dealing with large amounts of data in turbulence analysis, individual particles are processed while data analysis handles thousands of them. Statistical calculations on the particle velocities were made, and the root-mean-square (RMS) and mean velocities were calculated by the processor. Fast Fourier transform (FFT) analysis was calculated by the processor as well, which could be used to analyze the spectrum and correlation of the data. To ensure accurate analysis, it was essential to consider the random arrival of particles during the process [46]. Therefore, achieving a high data rate was of high priority during measurements. Although the measurements are of high accuracy, ensuring good statistical properties of the flow necessitated this approach.

Axial and radial velocity profiles were measured, with corresponding root mean square (RMS) values. Measurements were conducted across the length of the chamber, with special emphasis on the area above the swirler, as this area con-

tained the most important flow phenomena. The confidence interval for both mean and RMS values was computed for each measured point. By assuming normal distributed data, the following formula was used to calculate the confidence interval for the mean velocities [46]:

$$E = Z \sqrt{\frac{\bar{U}^2}{N}} \tag{3.1}$$

where $\bar{U}$ is the mean velocity, and N is the number of samples. A Z-value of 1.96 is used as the 95% confidence interval is calculated. For the remainder of the thesis E will be referred to as the Margin of Error (MoE). The velocity profiles were gathered at different heights above the burner in order to gain insight into how the flow field developed with increasing height. Profiles were gathered in both x- and y-directions to observe asymmetries.

With data on the recirculation zones, the total and recirculated mass flow rate was found through the equation [48]:

$$\dot{m} = \int_S \rho(U \cdot \vec{n}) dA, \tag{3.2}$$

where S is the surface and $\vec{n}$ is the normal vector. Since all mean axial velocities were normal to the surface in this case, $\vec{n} = 1$. Recirculated mass flow rates were separated in order to calculate the residence time in the recirculation zone.

3.6   Chemical Reactor Network (CRN)

A CRN was constructed in order to predict the NOx emissions from the burner
at different operating conditions. The model was a modified version of the model
constructed in the project assignment. A CRN can be used to complement exper-
imental results in order to get a better understanding of the combustion process.
Due to time constraints, conducting experiments with reactions was not feasible.
However, the CRN ensured that valuable insights could still be obtained from the
reacting flow case.

By integrating the velocity profiles with appropriate boundary conditions from
the experimental data, a mass flow rate could be calculated with corresponding
recirculation rates and residence times as mentioned in the previous section. The
calculated data was subsequently implemented into the model, which aimed to
address the limitations of CRNs in accurately representing fluid dynamic effects.

3.6.1   Cantera

Cantera v2.6.0 was installed as a library in Python 3.7, which is the framework in
which the model was built. It is an open-source software package that can perform
thermodynamic, transport equation, and chemical kinetics calculations [49]. To
model the chemical reactions taking place in the combustion chamber, various
types of reactors are represented by mathematical functions. These include PFRs
and PSRs, which provide governing equations for the relevant area of interest as
explained in Section 2.7. To simulate the reactions, one or more reactors can be
connected in a network and integrate the governing equations using the CVODES
solver, which is designed to handle stiff ordinary differential equations (ODEs)
[50]. In the subsequent sections, the most important parts of the model will be
explained in detail.

3.6.2 Overview of the model

The model consists of a Perfectly Stirred Reactor (PSR) and a Plug Flow Reactor (PFR). Its input is a reaction mechanism, the residence time of the reactors, the temperature of air and fuel, and pressure. Air and fuel are introduced separately and not mixed in the model to ensure that it represents a diffusion flame. Air was set to be composed of 20.8% O_2 and 79.2% N_2. One of the most critical factors in modeling a CRN is the choice of the reaction mechanism. As explained in section 1.3.2, the reaction mechanism is paramount in describing the chemical kinetics. The Okafor mechanism was chosen as the mechanism for this work, a reduced mechanism that is based on the GRI-mechanism 3.0 [17].

3.6.2.1 PSR

The initial region of the flame and the recirculation zone was modeled as a PSR, with the use of two ideal gas reactor functions. The PSR was suitable for the simulation of the initial region since the degree of mixing is high at the flame front [44]. It was modeled using mainly three classes from Cantera, which are briefly explained here [51]:

- Reservoir- A reactor held constant in its initial state.

- Mass Flow Controller (MFC)- Ensures a constant mass flow rate. Is not influenced by upstream or downstream conditions.

- Ideal Gas Reactor (IGR)- A reactor for ideal gas mixtures. 0-dimensional and held at a constant volume.
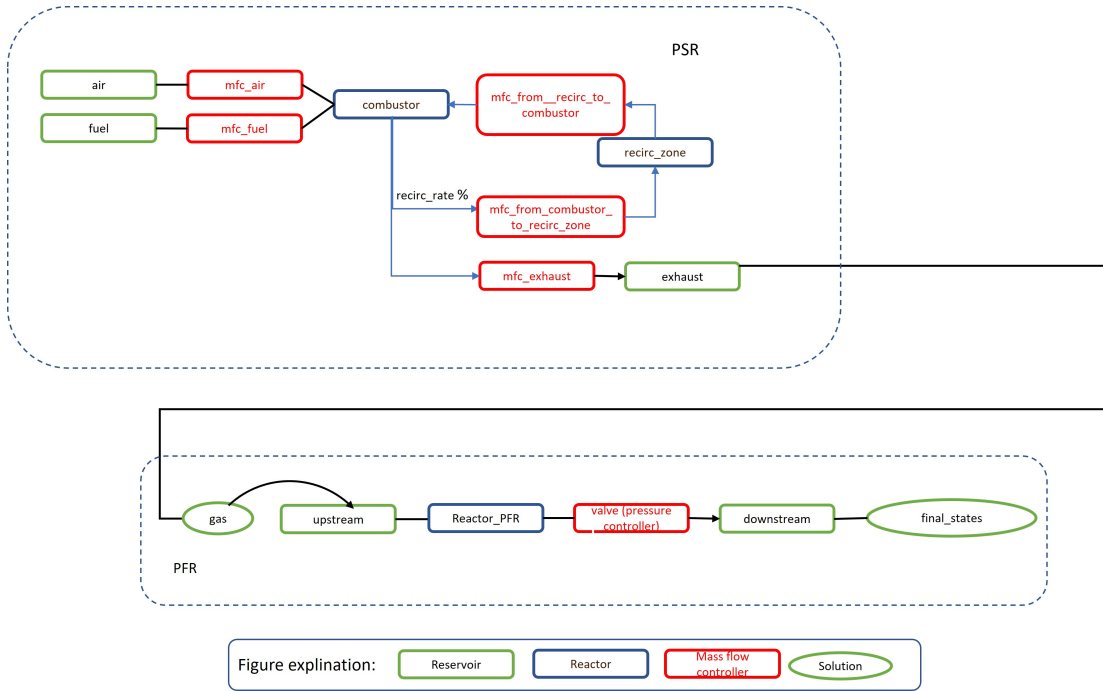
Figure 3.6: The overall structure of the script.

Two Reservoirs were defined which contained solutions of air and fuel separately. Secondly, two MFCs for the air and fuel were defined which ensured that the mass flow rate remained at its desired value. By not mixing the fuel and air and defining them as two separate MFCs, they preserved the physics of a diffusion flame. They served as input to an IGR, which in turn simulated the combustion. Further, two additional MFCs were defined which helped simulate the recirculation zone. The first was connected downstream to another IGR, which was connected upstream by the second MFC and subsequently connected to the first IGR, closing the loop. The states of the system could then be simulated, which in turn served as input to the PFR. This is illustrated in Figure 3.6, which shows the overall structure of the script.

3.6.2.2   PFR

The PFR served to represent the non-reactive section of the flame. This particular region can be characterized by lower thermal gradients compared to the initial flame section, where most reactions occur. Given its lower mixing degree due to a lower turbulence intensity, the use of a PFR to model this section was deemed appropriate [32]. The PFR was defined by connecting a Reservoir contain-

ing the simulated states from the PSR to an IGR which in turn was simulated. The simulated states represented the exhaust gas from the combustion process and contained useful information on the chemical states. When the simulation was completed, the concentration of NOx from the simulated exhaust (PFR) was extracted, plotted, and corrected for 15% dry O_2, through the formula:

$$\text{NOx}_{corrected} = [\text{NOx}] \cdot \frac{1}{1 - [\text{H}_2\text{O}]} \cdot \frac{0.208 - 0.15}{0.208 - [\text{O}_2] \cdot \frac{1}{1 - [\text{H}_2\text{O}]}}, \tag{3.3}$$

where the concentrations are extracted at the end of the PFR, and NOx is constituted of NO and NO_2 since the other species were of such small order of magnitude that including them would not have a large significance.

3.6.2.3   Validation

Simulated values were validated against measurements conducted by Ditaranto et al. [44] [52]. The mass flow rate of air was extracted from the data sets, and from these, the mass flow rate of fuel could be calculated using Equation 2.4. As noted by Ditaranto et al. [44], due to the nature of the diffusion flame the burner produce, the effective ER in the flame is close to stoichiometric conditions even though the overall ER is lean. For this reason, the mass flow rate of fuel was calculated assuming a stoichiometric ER.

3.6.3   Challenges

The project encountered several challenges throughout its duration. The primary obstacle was related to the traverse controller, which home position was as default set outside the physical limits of the rig. This meant that each time it was used it collided with the borders of the rig, damaging the apparatus. The issue proved hard to solve and persisted for a significant period until a solution was eventually found after correspondence with the manufacturer for several months. Furthermore, there were delays in producing and therefore assembling the burner and combustion chamber, resulting in a short timeline for conducting the experiments. As a result, it was not feasible to perform experiments involving a reacting flow as initially planned, and cold flow measurements with the burner did not start until

Easter 2023. Therefore, a decision was made to replace what was initially planned to be measurements with a reacting flow with a modified CRN model used during the project work.

FOUR

RESULTS AND DISCUSSION

The results from the Laser Doppler Velocimetry (LDV) measurements and the simulations using the Chemical Reactor Network (CRN) will be presented in this chapter, along with a comprehensive discussion of the obtained results.

4.1   Laser Doppler Velocimetry Measurements

This section provides a comprehensive characterization of the mean flow field above the swirl-stabilized burner. Detailed analyses of both axial and radial velocities are undertaken, with corresponding root mean square (RMS) values examined. Special emphasis is taken to identify and quantify any recirculation zones present. The implications of these results are discussed, clarifying the dynamic behavior of the flow field.

4.1.1   Mean flow field

Figure 4.1: Mean axial velocity profiles at increasing heights above the burner tip. The measurements were conducted along $y = 0$ mm.

Figure 4.1 display the mean axial velocities across the combustion chamber at three different heights. In the context of this analysis, $h = 0$ mm refers to the position level with the tip of the burner. As the height h increases, this indicates movement further downstream from where the jet is ejected from the tip. The coordinates x and y denote the Cartesian coordinates constituting the horizontal plane with respect to the combustion chamber. The point $(x, y) = (0, 0)$ is defined to be at the center of the burner tip.

Figure 4.1 display the mean axial velocities across the combustion chamber at three different heights. Within -20 mm $\leq x \leq 20$ mm hereby referred to as the area above the burner, the resolution of the measurements were high. This increased resolution was necessary due to the presence of large velocity gradients

in this particular area. Conversely, for areas outside of this specified range, the measurements were made with lower resolution since velocity gradients in these regions were not as pronounced At $h = 30$ mm, flow retardation is present from $x = -5$ mm to $x = 9$ mm. This indicates the onset of an Internal Recirculation Zone (IRZ) due to the swirling air ejected from the center of the burner. The lowest mean velocity in this region ($U \approx 23$ m/s) is 53% of the jets maximum velocity ($U_{max} \approx 43$m/s) indicating significant flow retardation at this height. The swirl intensity was however not strong enough to induce negative velocities and hence recirculation in this area. The lowest mean velocity in this region is located at heights $h = 40$ mm and $h = 60$ mm, and are 69% and 77% percent the value of their maximum jet velocity respectively. At $h = 60$ mm, the flow retardation has weakened significantly.

The stagnation points of the mean axial velocity where $U = 0$ m/s is an indication of the outline of the recirculation zones [13], and can be used to identify them. At $h = 30$mm, a recirculating zone is present between -50mm $\leq x \leq -15$mm, where $U = 0$m/s. This is due to the presence of two counter-rotating vortices, one with a positive direction of rotation which is centered around $x = -15$mm, and one with a negative direction of rotation which is centered around $x = -50$mm. At $h = 40$mm a recirculating zone is present between -50 mm $\leq x \leq -19$ mm. The magnitude of the negative velocities is smaller than at $h = 30$ mm, indicating weakened recirculation in this zone. However, at $h = 60$ mm no recirculation is present. Recirculation being present at only the left side of the chamber ($x < 0$ mm) could be due to the asymmetric burner configuration. As discussed by Cozzi et al. [8], swirling flows are sensitive to asymmetries in the configuration. It can lead to intermittent flow reversals that are not observable in the mean velocity field, which could potentially lead to any recirculation present at the right side of the chamber not being captured by the mean flow field.
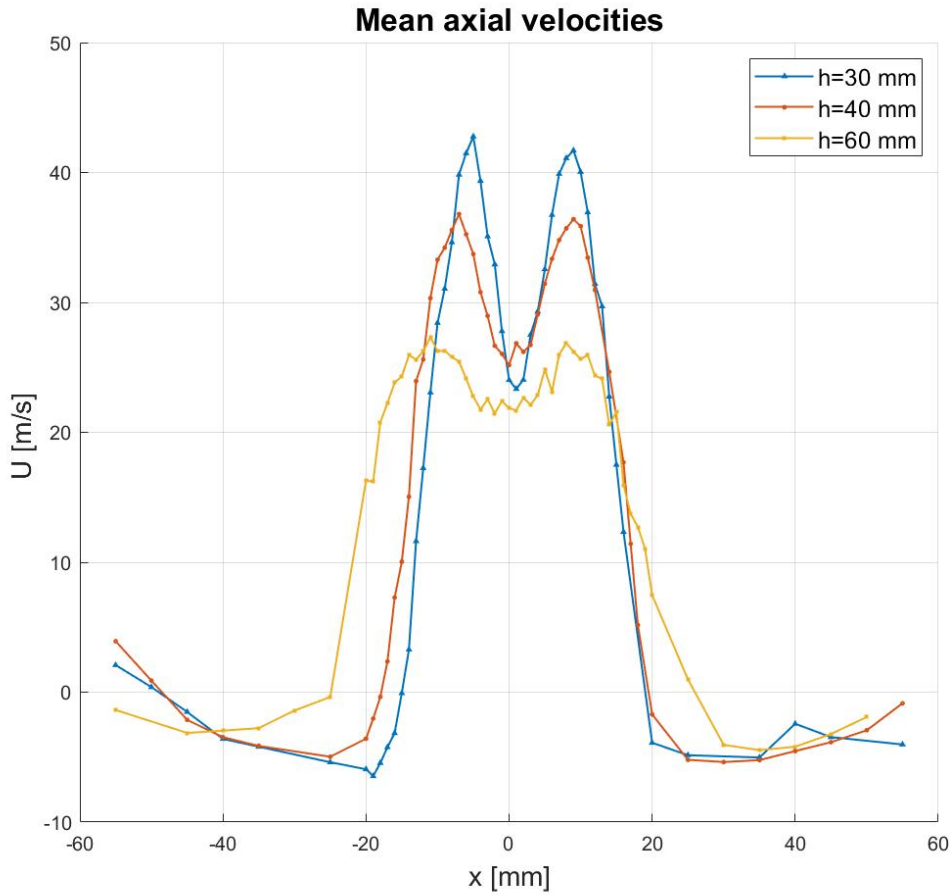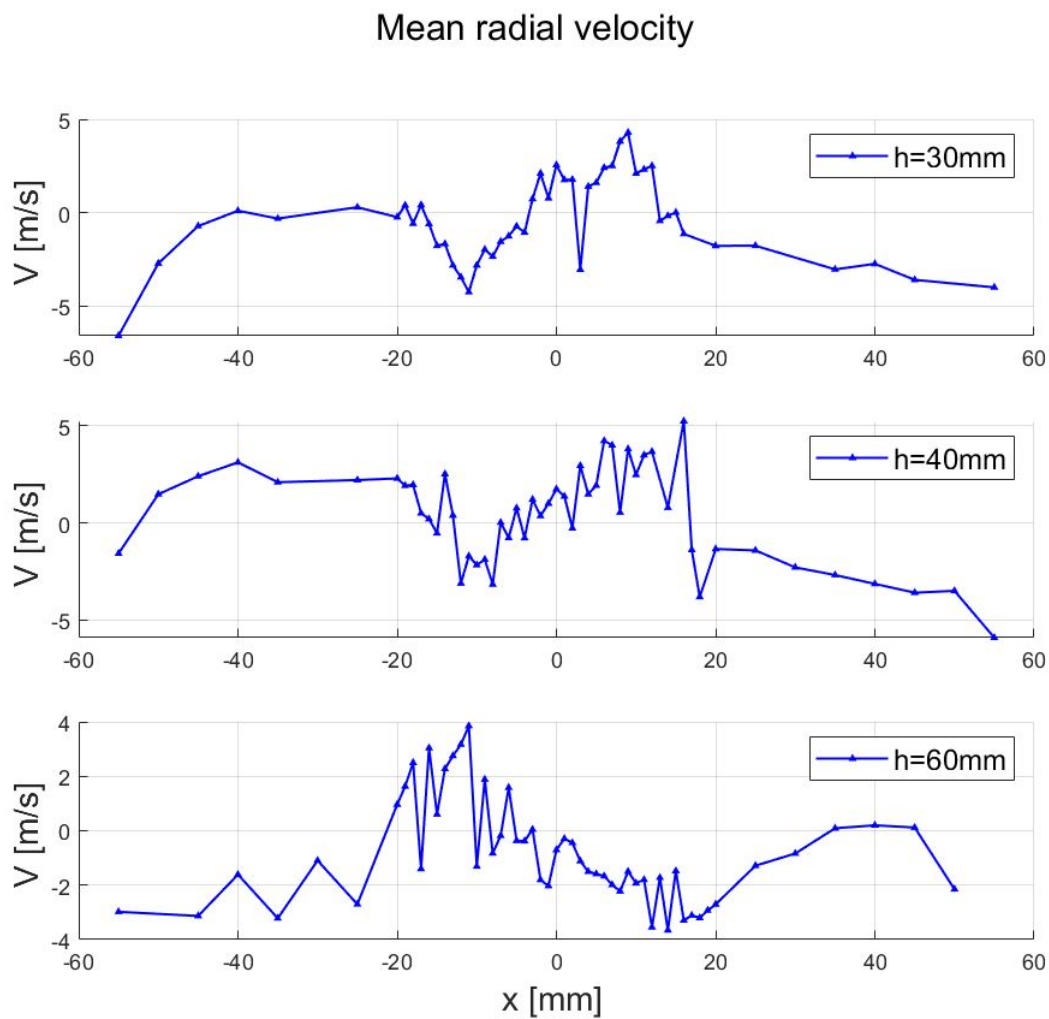
Figure 4.2: Mean radial velocity profiles at increasing heights above the burner tip. The measurements were conducted along $y = 0$ mm.
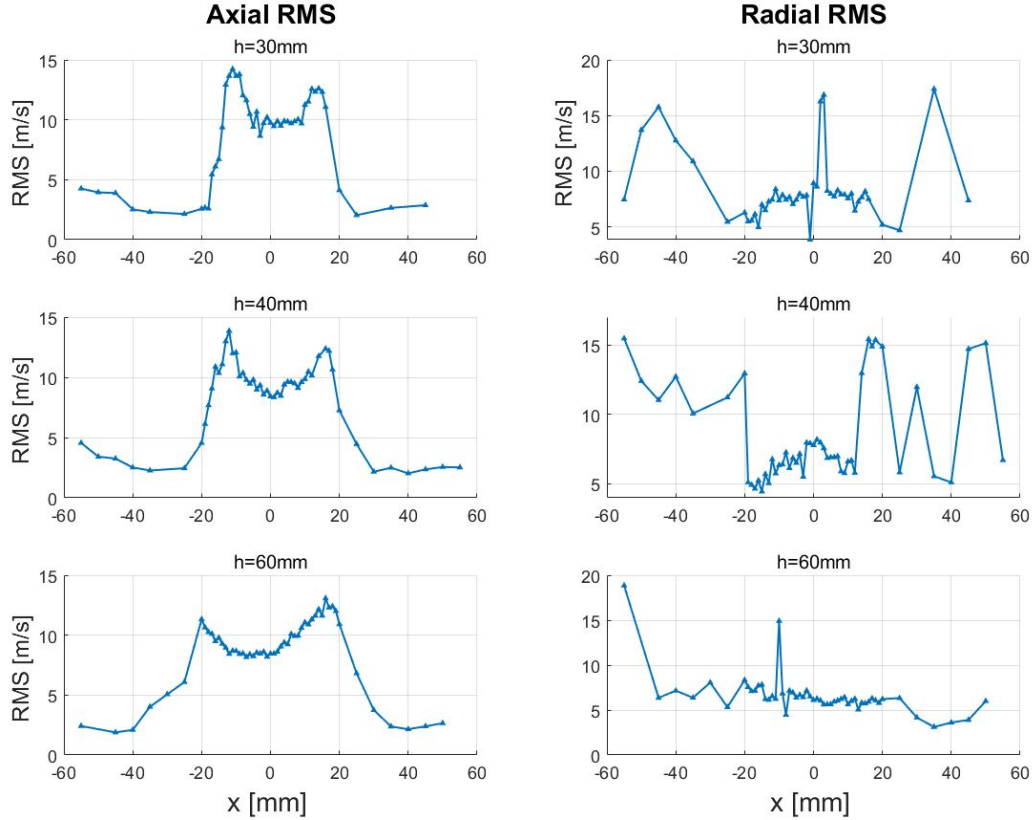
Figure 4.3: RMS plots. Measurements of the axial RMS are plotted in the left column, while the radial RMS is plotted in the right column as a function of the chamber width. Measurements are conducted along $y = 0\,\mathrm{mm}$.

The mean radial velocity is displayed in Figure 4.2. At $h = 60$ mm, the mean velocity is mainly positive from $x = -20$ mm to $x = -3$ mm, although significant fluctuations are occurring. This can be an indication of high turbulence levels in the flow in this region. From $x = -3$ mm to $x = 20$ mm the mean velocity is mainly negative. This indicates that the air is injected towards the jet core, entraining surrounding ambient air. If combustion was occurring, the mixing of hot combustion products and cold surrounding air could lower the flame temperature and therefore reduce NOx emissions. Measurements above the swirler at $h = 30$ mm and $h = 40$ mm demonstrate that air is ejected radially from the jet core as shown in Figure 4.2.

In Figure 4.3 the RMS values are plotted as a function of the chamber width. Large spikes in the values can be seen at all heights. At $h = 60$ mm the spike that occurs at $x = -50$ mm can be attributed to the fact that the MoE is relatively

high at this point compared to others ($E = 1.95\%$), however for the rest of the spikes this is not the case. They can be indications of instabilities in the flow at these locations. At $h = 30$ mm and $h = 40$ mm, they are mainly located outside the area above the burner. The instabilities in these regions indicate the presence of ORZs. The fact that the radial RMS at $h = 60$ mm is comparatively flat, is a sign of no recirculation being present at this height.

The axial RMS profiles exhibit pronounced peaks at the edges of the area above the burner, indicating local mixing in the shear layer between the jet and the surrounding ambient air. This finding is consistent with the observations of Meier et al. [13]. The axial RMS declines by $\approx 20\%$ at its left maxima from $h = 30$ mm to $h = 60$ mm, however at its right maxima the value is indicated to increase by $\approx 6\%$. This trend can signify that the momentum of the jet is higher on the right side of the chamber compared to the left. As indicated in Figure 4.1, two vortices creating a recirculation zone are present in this area, which could add momentum to the jet.
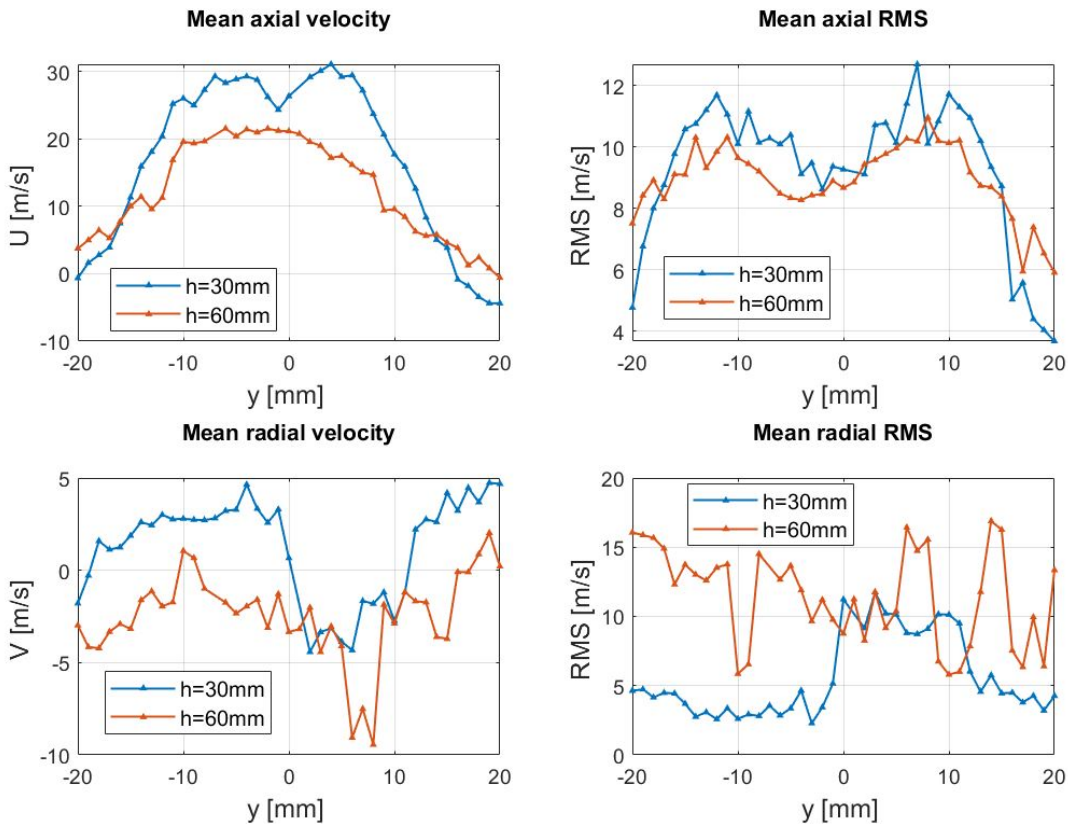
Figure 4.4: Mean axial and radial velocity with corresponding RMS along $x = 0$ mm.

High-resolution measurements of the mean axial velocity were conducted along the $x = 0$ mm axis, in order to understand how the recirculation zones affected this area of the flow as shown in Figure 4.4. At $h = 30$ mm a flow retardation is evident from $-4\,\text{mm} \leq y \leq 3\,\text{mm}$, albeit weak when compared to the retardation occurring in the x-direction. Higher up in the flow field, at $h = 60\,\text{mm}$ the velocity profile resembles that of an ordinary flat-top turbulent jet in this particular area. The radial velocity is predominantly positive, however, it turns negative between $-0\,\text{mm} \leq y \leq 12\,\text{mm}$ which means that air is being entrained towards the jet core at $y = 0$ mm. At $h = 60$ mm, the majority of radial velocities are negative, implying an inward-directed airflow towards the left side of the chamber. This may suggest the existence of a flow structure in this region, although definitive conclusions are challenging to draw without measurements being conducted in the region. Moreover, a pronounced dip in velocity is observed within the range of $5\,\text{mm} \leq y \leq 10\,\text{mm}$, coinciding with an elevated RMS value. This implies the occurrence of flow instabilities within this specific region.

Figure 4.5: Mean axial velocity profiles along $y = 0$ mm. For $h = -20$ mm and $h = 0$ mm. Measurements could only be conducted to $x = -41$ mm as this is the position where the edge of the burner was located.

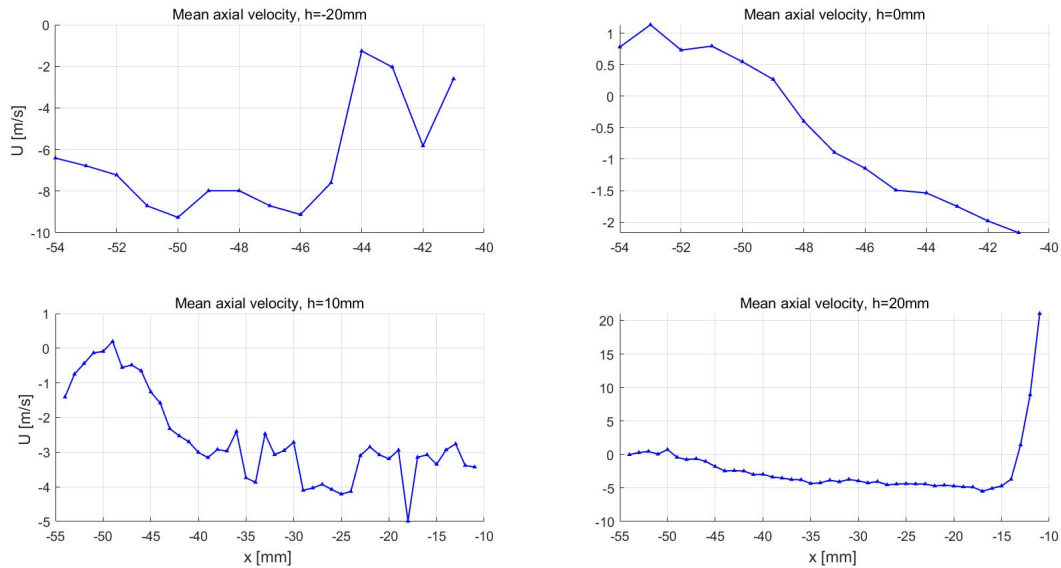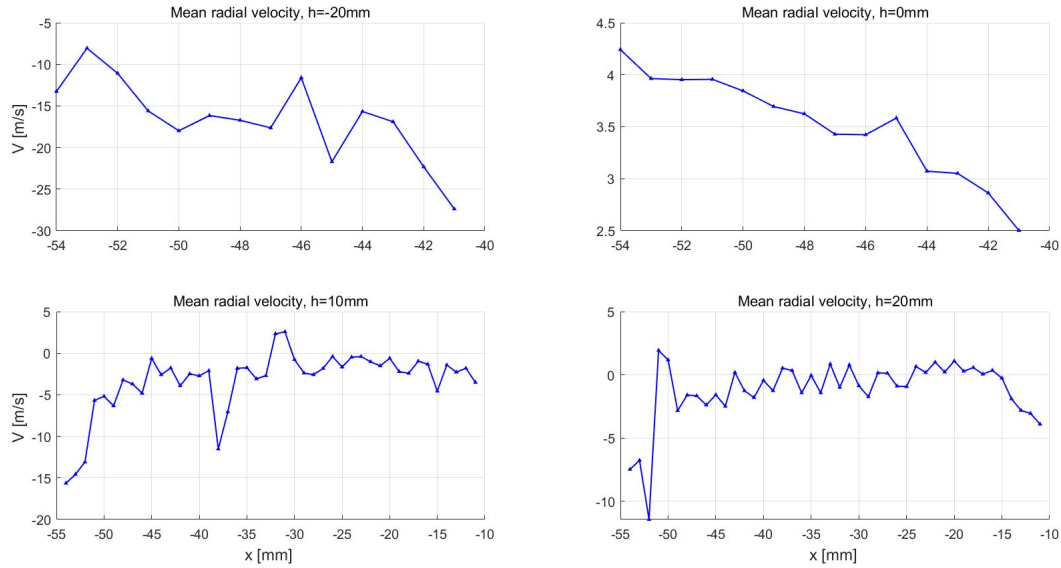**Figure 4.6:** Mean radial velocity profiles along $y = 0$ mm. For $h = -20$ mm and $h = 0$ mm measurement could only be conducted to $x = -41$ mm as this is the position were the edge of where the burner was located.

4.1.2   Near field measurements

Measurements were systematically carried out along the main air hole at $y = 0$mm, at a height $h = -20$ mm directly level with the burner tip surface, at $h = 0$ mm, as well as at elevations $h = 10$ mm and $h = 20$ mm above the burner. All these measurements were conducted specifically on the left side of the chamber. By the main air holes, the mean axial velocity is significantly more negative compared to the profile at $h = 0$ mm, shown in Figure 4.5. A possible reason for this is due to the high radial velocity of the air ejected from the main air holes as shown in 4.6, which has a global mean velocity of $V = -16.6$ m/s for the entire profile. The high magnitude velocity will create a low-pressure zone across the chamber at this height, which can create local suction that draws in air from above. This will then in turn result in large negative mean axial velocities. There are however no positive velocities present, meaning no recirculation is present. Recirculation is observed at $h = 20$ mm, in the region between -50 mm $\leq x \leq -13$ mm as stagnation points are present. At $h = 0$ mm and $h = 10$ mm, a stagnation point is present near $x = 49$ mm. Even though measurements are not conducted to the center of the burner, the velocity is known to turn positive somewhere in this

region. Therefore, recirculation is present at both heights.

At $h = 0\,\text{mm}$ the mean radial velocities are positive, which means that air is being drawn in towards the jet core. At $h = 10\,\text{mm}$ and $h = 20\,\text{mm}$, the radial velocities are fluctuating, indicating a high degree of turbulence. The enhanced mixing, due to this and the presence of the recirculation zone in the region, would contribute to flame stabilization in the reactive flow case. It would do so by continuously delivering fresh cold air to the reactants in the flame front.
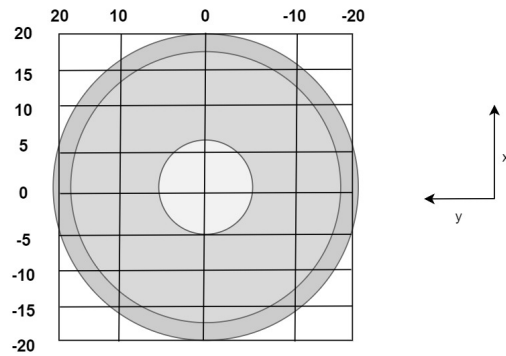
Figure 4.7: Figure illustrating the mesh that the traverse controller conducted measurements in above the burner. Measurements were made 30 mm and 60 mm above the burner tip surface.

4.1.3 Planar velocity fields

Planar mean axial velocity fields above the burner were constructed by taking measurements of the mean axial velocity in a mesh as seen in Figure 4.7. By interpolating values between the measured positions, planar velocity fields were constructed 30 mm and 60 mm above the burner tip. Similar velocity fields were constructed for the mean radial velocities.

Figure 4.8: Planar axial velocity field at a height $h = 30$ mm above the burner.
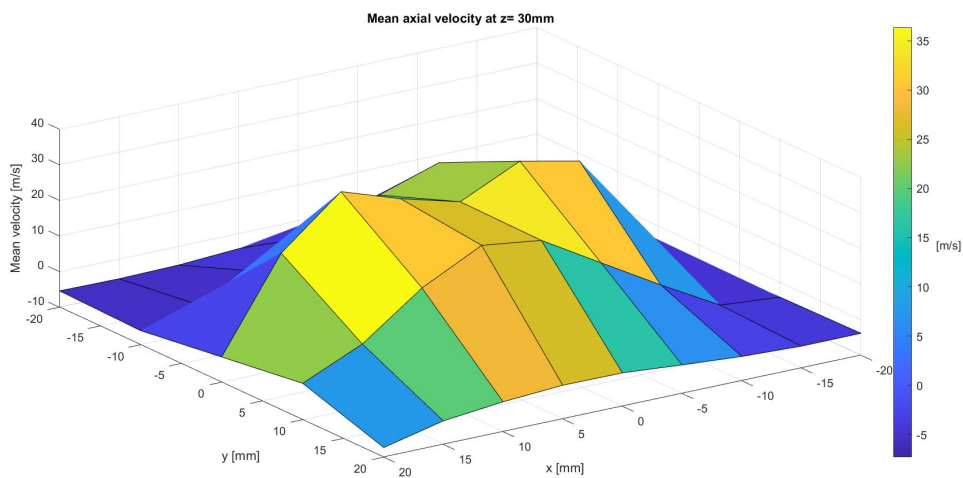
Figure 4.9: Planar axial velocity field at a height $h = 30$ mm above the burner.
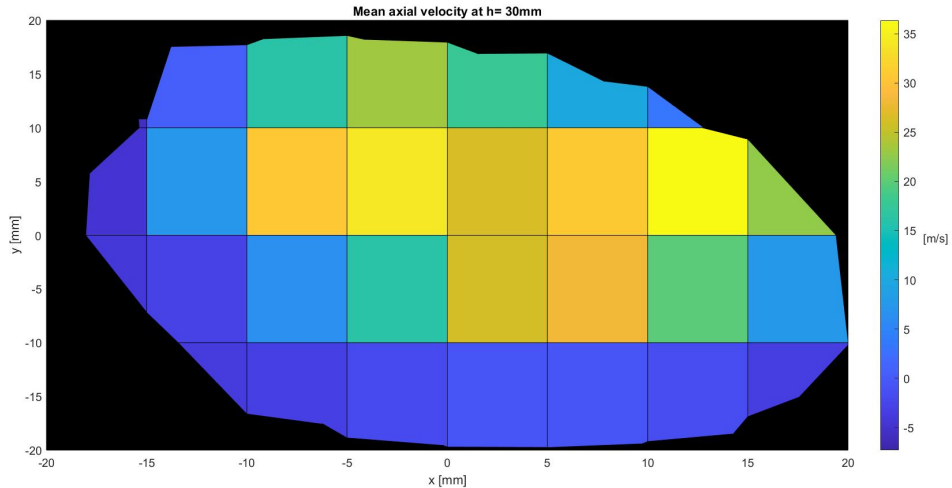
Figure 4.10: Contour plot of the velocities at $h = 30$ mm. The black section shows the negative velocities in the axial velocity field. The border between the black section and the tiled section illustrates the isoline of where the velocity turns negative.

The planar velocity fields measured at $h = 30$ mm are shown in Figures 4.8 and 4.9. It can be observed that the flow field is highly asymmetrical, with mean velocities that are predominantly negative between $-20\,\text{mm} \leq y \leq -10\,\text{mm}$, while between $10\,\text{mm} \leq y \leq 20\,\text{mm}$ the mean velocities are predominantly positive. This emphasizes the asymmetry of the flow field, which is likely due to a combination of the asymmetrical configuration as well as the complexity of the swirling flows.

Additionally, a contour plot was made at $h = 30\,\text{mm}$ with an isoline showing where the mean velocity turns negative, which can be seen in Figure 4.10. Without measurements extending to the chamber walls, no conclusion can be made of whether they are the outline of a large recirculating structure which would be indicated by a turn from negative to positive velocities in this region. However, with knowledge from measurements conducted along $x = 0\,\text{mm}$, it can be assumed that a recirculating zone is present for negative x-values, but not for positive x-values.
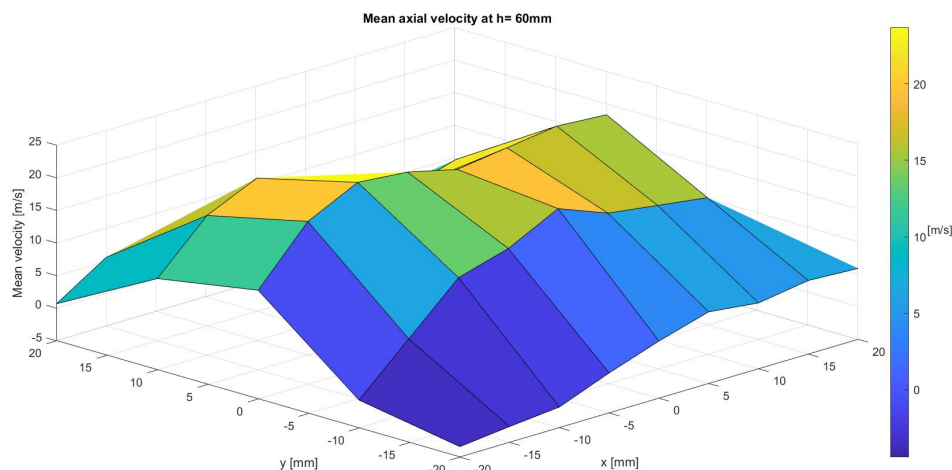
Figure 4.11: Planar axial velocity field at a height $h = 60$ mm above the burner.
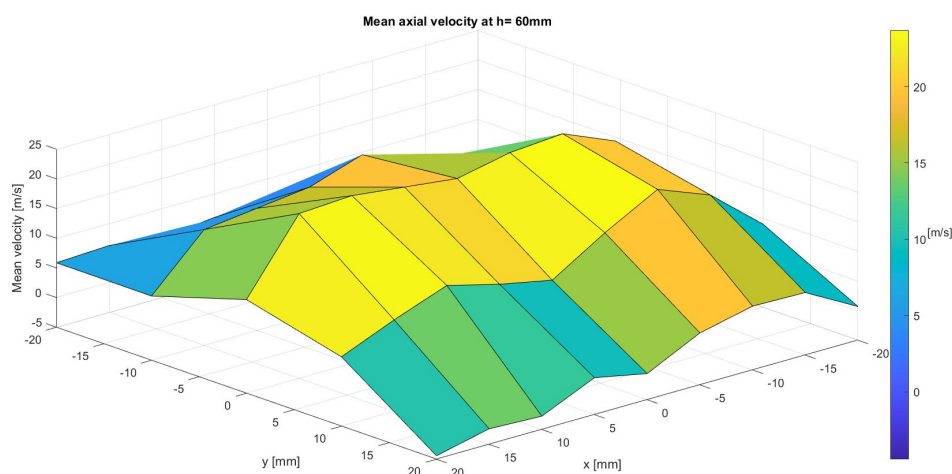
Figure 4.12: Planar axial velocity field at a height $h = 60$ mm above the burner.

The measurements taken at $h = 60$ mm are shown in Figures 4.11 and 4.12. Negative velocities are only present from $y = -10$ mm to $y = -20$ mm, demonstrating that the flow field is still asymmetric at this height. Additionally, the gradients are less steep compared to $h = 30$ mm which displays that the spreading rate of the jet has increased substantially. The lower velocities in this area will in effect cause the turbulence levels to be lower, and mixing less pronounced. Due to this, it can be argued that it is appropriate to model this region as a PFR in the case of a reacting flow field as discussed in Section 3.6.2.2
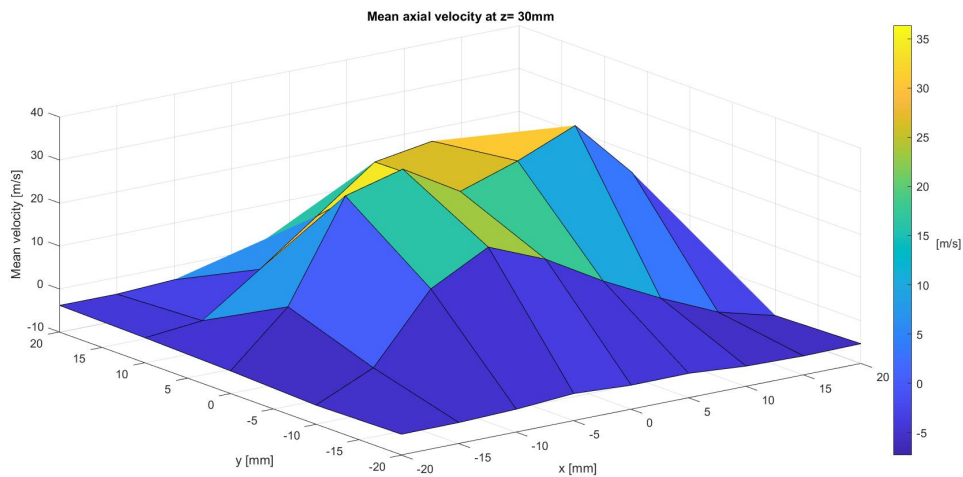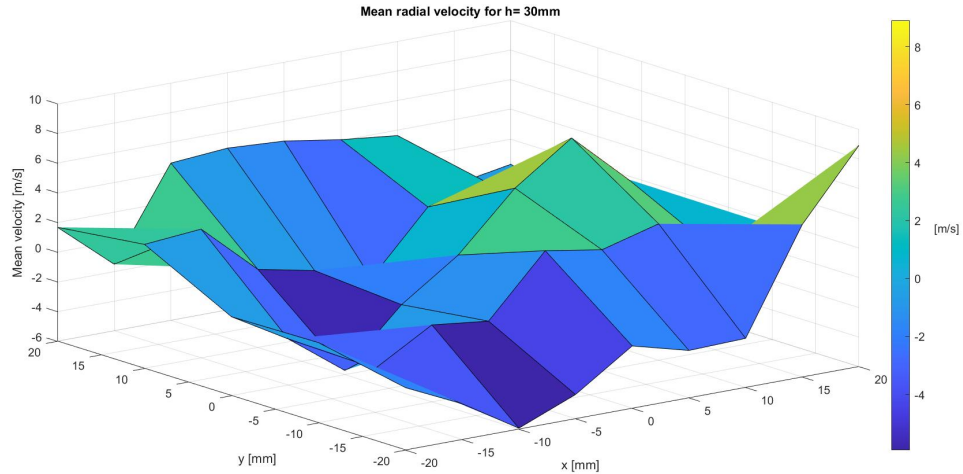
Figure 4.13: Planar radial velocity field at a height $h = 30$ mm above the burner.
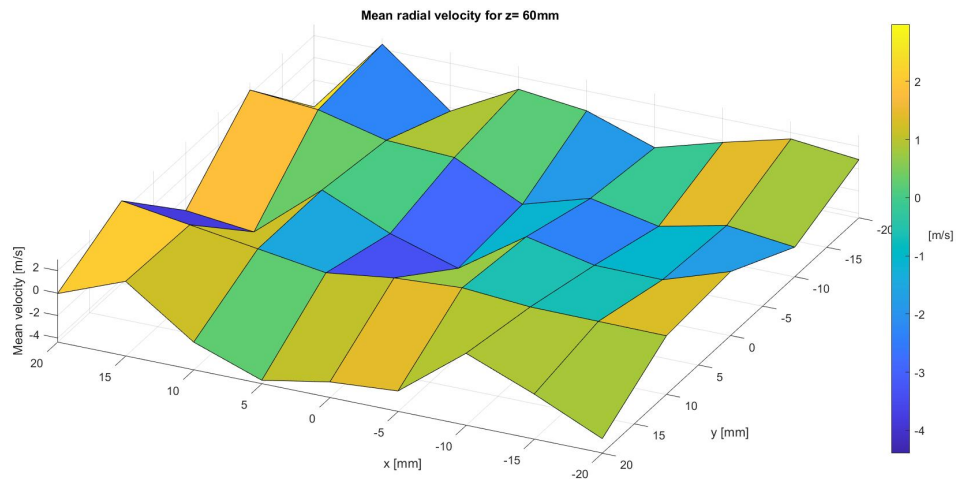
Figure 4.14: Planar radial velocity field at a height $h = 60$ mm above the burner.

In Figure 4.14 and 4.14 a planar velocity field of the radial velocity is shown. Larger velocity magnitudes and gradients can be observed at $h = 30$ mm than at $h = 60$ mm, which indicates that a larger amount of air is being entrained in this part of the velocity field. Along $y = 0$ mm at $h = 30$ mm, the largest mean velocities are found. The mean velocity has a positive gradient from $x = -10$ mm to $x = 10$ mm in this region, while along $x = 0$ mm, a negative gradient is present from $y = -10$ mm to $y = 10$ mm. They both indicate that air is being entrained toward the jet core. As noted by Pope [33, p.102] this is expected at the edges of a turbulent jet. This is an indication that the jet behaves as expected in this

region, and no recirculating zones are present in the region.

4.1.4   Determination of the volume of the recirculation zone and residence times

Not enough data points to determine the exact volume of the recirculation zone, however, an estimation could be made by using the mean velocity isolines and stagnation point as an indication of the outline of the recirculation zone at the different heights. From this, a volume could be constructed. The data obtained indicated the presence of an ORZ present at the left side of the chamber between $0 \, \text{mm} \leq h \leq 40 \, \text{mm}$, however, no evidence of an ORZ on the other side of the chamber, or an IRZ was found. Data at $h = 60 \, \text{mm}$ indicated that no recirculation is present at this height along $y = 0 \, \text{mm}$, and even though it is possible for a recirculation zone to be present along other y values, it is assumed that there is no recirculation in the axial direction given the available data.

The assumed volume of the PSR was taken to be the total volume of the chamber the in the region between $0 \, \text{mm} \leq h \leq 40 \, \text{mm}$ since this was the assumed height of the ORZ. In turn, this was subtracted by the volume of the recirculation zone, since this would give an approximation of the initial region of the flame in the combusting case. This is likely an overestimation, as a significant volume is occupied by the mixing of reactants and cold air. The actual volume of the PSR is where stoichiometric conditions are achieved and combustion happens. However, to accurately estimate this volume, the thickness of the flame front is required, which was not obtainable with the cold flow data available.

By using the mass flow rate found at $h = 30 \, \text{mm}$, a residence time for the PSR and the recirculating zone was found. By integrating the velocity field measured in Figure 4.8, the mass flow rates could be found through Equation 3.2. The residence time in the PSR and ORZ could subsequently be found through Equation 2.21. A recirculation rate could be found as well, by dividing the recirculated mass flow by the total mass flow.

Table 4.1: Calculated values from LDV measurements

Quantity	Value
τ_{PFR}	0.248 [ms]
τ_{PSR}	0.227 [ms]
τ_{recirc}	0.274 [ms]
Recirc rate	0.15 [-]

The volume of the PFR was calculated as the remaining volume of the chamber downstream of the ORZ. Although it was not a complete description of the flow field at this height, it was deemed representative with the data at hand. The mass flow rate found at $h = 60$ mm was deemed to be representative of the mass flow rate in the PFR. There is an incompleteness to some of the data sets as they do not extend to the chamber walls, and the total recirculated mass flow is likely higher than the values found. This needs to be kept in mind when interpreting the results of the CRN. The results are summarized in Table 4.1, and with these quantities determined, simulations with the CRN could commence.

4.2 Chemical Reactor Network Simulations

Simulations of combustion using pure H_2/air and pure CH_4/air mixtures were conducted using the CRN model. The reliability of this model was validated against the findings from previous experimental studies carried out by Ditaranto et al. [44] [52]. These referenced experiments, performed under both differing and identical conditions to the cold flow experiments on the same burner, served as benchmark data for validation purposes. Additionally, simulations of increasing pressures were performed to observe if the model could be scaled to higher pressures. High-pressure experiments in combustion chambers are difficult to perform, therefore it is useful to have models that can accurately predict emissions.

4.2.1   Comparison between measured and simulated values

Simulations were performed for similar conditions during the experiments, with inlet parameters in the model as shown in Tables 4.4 and 4.2. The resulting NOx concentrations corrected for 15% dry O_2 are shown in Table 4.3 as Case 1.

Table 4.2: Values of pressure and temperature and mass flow rate of fuels for cases 1 and 2 in the CRN.

Case	Temperature air and fuel, T[K]	Pressure, p [bar]	$\dot{m}_{CH_4}\ [g/s]$	$\dot{m}_{H_2}\ [g/s]$
1	298.15	1	0.267	0.135
2	298.15	1	0.397	0.201

The concentration was predicted to be 21ppm with CH_4 as fuel, while the measured value from previous experiments was 18 ppm. This yields an absolute error of 3 ppm which is a slight overestimation. It could be due to the fact that the model does not account for heat losses to the chamber walls, which could reduce the flame temperature and therefore NOx emissions. As noted by Turns [19, p.506], turbulent diffusion flames can be highly radiating.

Table 4.3: NOx emissions from the different cases corrected for dry 15% O_2.

Case	Simulated value, H_2 fuel [ppm]	Measured value, H_2 fuel	Simulated value, CH_4 fuel [ppm] el	Measured value CH_4 fuel
1	26	17	21	18
2	26	28	21	24

Table 4.4: Table of the inlet parameters used in the CRN for case 1 and case 2.

Inlet parameters	Value
$T_{0,fuel}$	293.15 [K]
$T_{0,air}$	293.15 [K]
p	1 [bar]
τ_{recirc}	0.274 [ms]
τ_{PSR}	0.227 [ms]
τ_{PFR}	0.248 [ms]
Recirculation rate	0.15 [-]

Meier et al. [6] conducted experiments on a swirl burner operating at similar conditions ($P = 10.3$ kW, ER=0.75) utilizing CH_4 as fuel, and reported NO concentrations of 25 ppm being present in the exhaust gas. As most of the NOx predicted by the CRN is constituted of NO, which will be discussed in the subsequent section, the reported value is close to the one obtained from simulations, however slightly higher. This can likely be attributed to the fact that the flame is

operated at 300 W higher power, in addition to differences in the configuration. It is however further indication that the model is able to perform satisfactory predictions at similar operating conditions with CH_4 as fuel.

With H_2 as a fuel the measured value of NOx emissions was 17 ppm, while the predicted value of the CRN was 26 ppm. This is a significant overestimation and can be caused by several factors. One is the mechanism chosen for the CRN, which is developed for primarily natural gas combustion and not hydrogen combustion. Another is due to the fact that the calculated values for the residence times are calculated for cold conditions, and will not account for the volumetric expansion occurring during combustion which will likely increase the size of the recirculation zone as discussed by Dutka et al. [12]. The volumetric expansion effect can be expected to be more significant when H_2 is utilized as a fuel due to its higher flame temperatures compared to CH_4 at the same conditions.

Additionally, the high diffusivity of H_2 is not accounted for in the CRN meaning it will not capture the effect of increased mixing due to this. The increased mixing due to an increased size in recirculation zone and high diffusivity could improve the mixing of cold surrounding air with hot products and effectively reduce the temperature and NOx emissions. These effects are however not captured in the CRN. Additionally, instabilities in the flow field could be present that cause periodic fluctuation that influences the size of the recirculating zone are not modeled by the CRN, and could have an effect on the formation of NOx. This was found to occur in a methane flame operated at a similar power output [13].

Simulations were conducted at the same temperature and pressure at elevated mass flow rates as well (Case 2), corresponding to a power output of 15 kW. The mass flow rate of air was in this case $\dot{m}_{air} = 6.87$ g/s. As displayed in Table 4.3, the predicted NOx emissions when using CH_4 had an absolute error of 3 ppm when compared to the measured values, while for H_2 the absolute error was 2 ppm. This indicates the model can handle relatively small changes in mass flow rate at similar conditions well, and it is in fact better for the case with H_2 as a fuel. This may be due to the fact that the size of the recirculation zone is too small

when using non-reacting flow data in the model, however, when the mass flow rate is bigger the values calculated are more representative due to the volumetric expansion occurring during combustion of H_2.

For methane the model corresponds well for both cases, indicating that the non-reacting flow measurements are representative when it is used as fuel. Simulated values using H_2 as fuel were not satisfactory at similar conditions, which warrants further investigations into the residence times used for the fuel. The predicted values are however very similar to those predicted for Case 1, indicating that the model has a low sensitivity towards the mass flow rates. Parameters such as residence times, temperature, and pressure proved to be more influential on the results of the simulations.
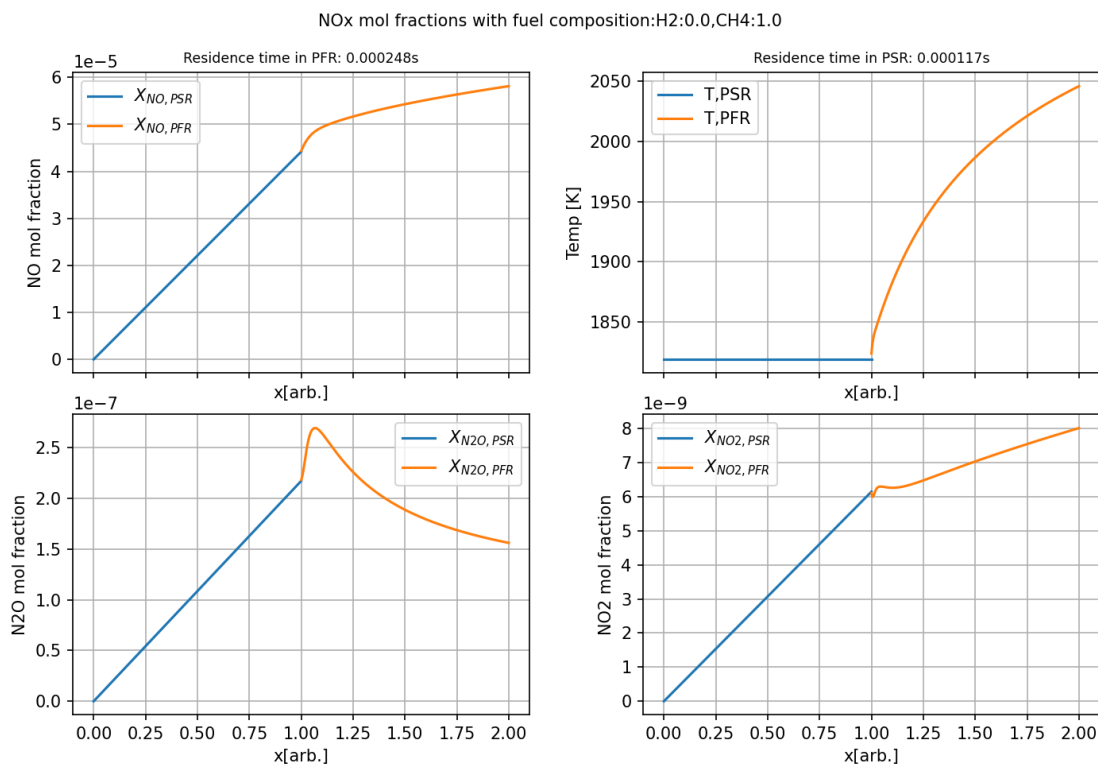
4.2.2 Evolution of species and temperature

Figure 4.15: Plots of the concentrations of NO,NO_2, N_2O and temperature in the PSR and PFR.
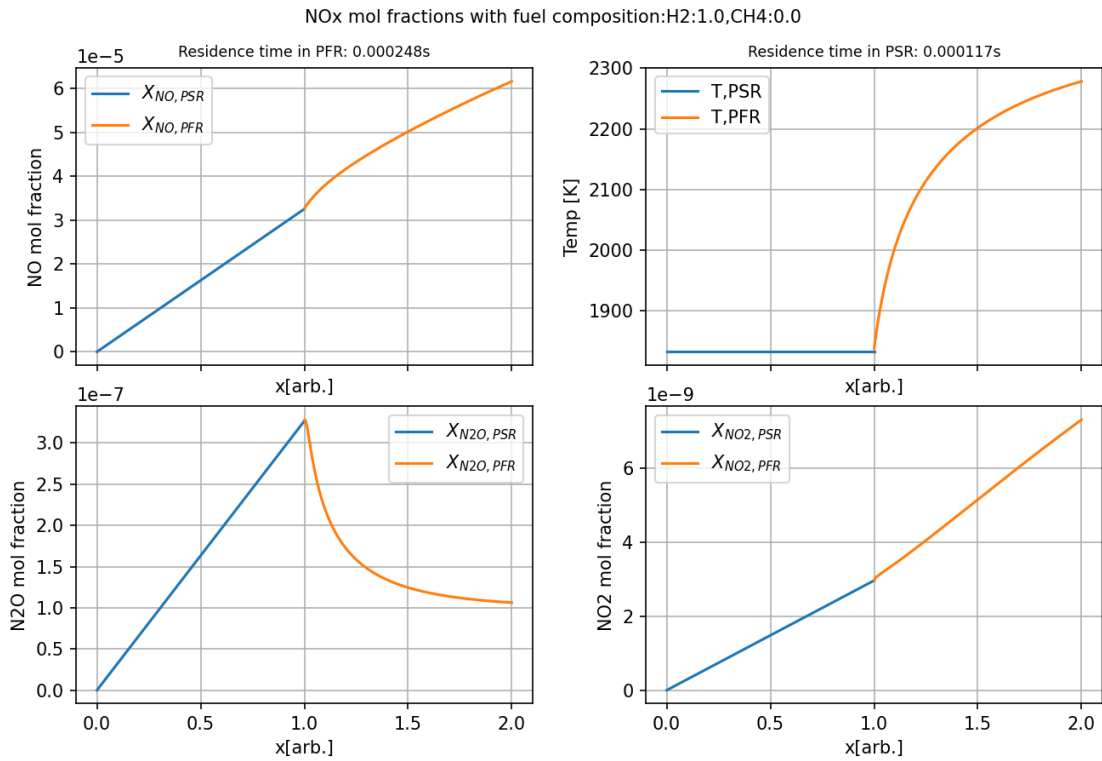
Figure 4.16: Plots of the concentrations of NO,NO$_2$, N$_2$O and temperature in the PSR and PFR.

The evolution of NO, NO$_2$, N$_2$O and temperature simulated by the CRN at similar conditions to the experiments are shown in Figures 4.15 and 4.16. It can be observed for both cases that the main part of the predicted NOx emissions is constituted by NO, which is 2 orders of magnitude larger than the second largest contributor N$_2$O. NO is formed at a larger degree in the PFR when H$_2$ is the fuel, due to the higher flame temperature present. Additionally, N$_2$O is consumed more rapidly with H$_2$ as a fuel than with CH$_4$. One of the reasons for this may be due to the fact that the SZ of the combustion which the PFR is modeling, has a higher temperature than the PZ, which may not be favorable for the N$_2$O-mechanism as discussed in section 2.4.5. NO$_2$ is formed at low levels with both fuels. This indicates that the main contributor to the predicted NOx emissions is thermal NO formation, which is expected in the high-temperature combustion of gas fuel [16]. Additionally, the model predicts a higher flame temperature for H$_2$ than for CH$_4$ as fuel, which leads to higher NOx emissions through thermal NO formation which is in agreement with established literature.
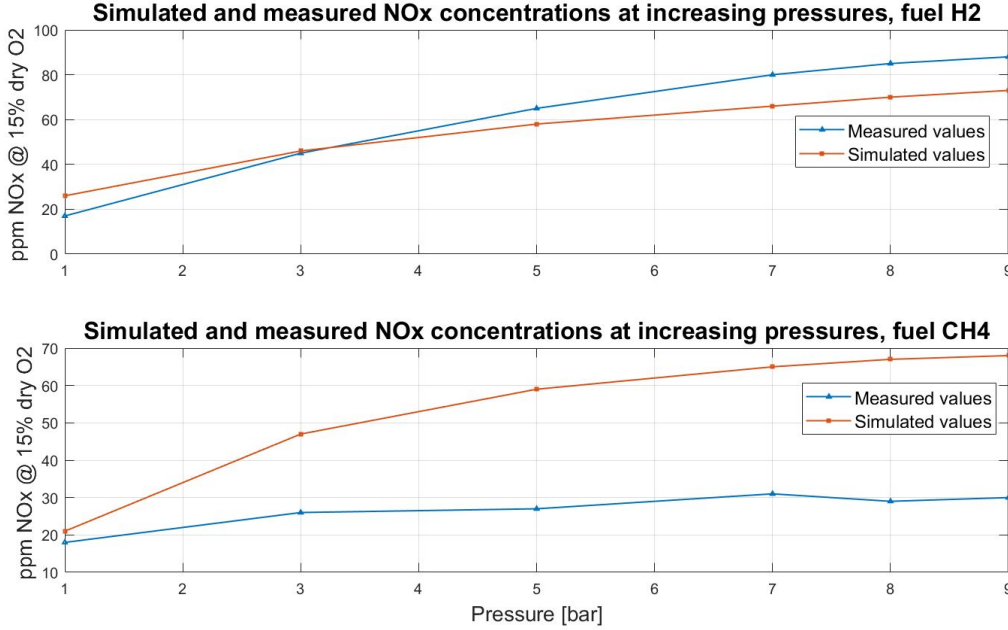
Figure 4.17: NOx concentrations as a function of pressure for measured and simulated values.

Table 4.5: Mass flow rate of fuel and air for different pressures.

Pressure [bar]	$\dot{m}_{CH4}$[g/s]	$\dot{m}_{H2}$ [g/s]	$\dot{m}_{air}$, fuel H_2 [g/s]	$\dot{m}_{air}$, fuel CH_4 [g/s]
1	0.27	0.13	4.6	4.6
3	2.38	0.38	12.96	40.94
5	5.26	0.63	21.55	90.50
7	10.76	0.89	30.13	185.12
8	13.39	1.01	34.48	230.17
9	16.25	1.14	38.83	279.45

4.2.3   Effect of pressure

The results of the model were compared to the measured values with increasing pressure with CH_4 and H_2 as fuel with a constant temperature of $T_{air} = T_{fuel} = 293.15\,\text{K}$ with the aim to validate the model at higher pressures. The same values for residence times and recirculation rate found by the LDV measurements were used. The results are displayed in Figure 4.17, and the mass flow rates for the different pressures are shown in Table 4.5. The rest of the inlet parameters with an exception to the pressure is identical with those in Table 4.4. With H_2 as fuel, the predicted values match well at $p = 3\,\text{bar}$ however, at higher pressures, the values deviate and predict lower NOx emissions. As the mass flow rate is increased

compared to the cold flow, turbulence intensities are expected to be stronger and recirculation zones are expected to be larger. This may lead to increased residence times, and therefore longer time to reach chemical equilibrium resulting in increased formation of NOx. Measurements of the flow field at these flow rates would therefore be needed. The model does however capture the trend of increasing pressure, indicating that the model is working as intended, but parameter values may cause it to deviate.

With CH_4 as a fuel, there are large deviations at all pressures except at $p = 1\,\mathrm{bar}$. The model over predicts the NOx emissions significantly, which can be caused by several factors. The increased mass flow rates are likely to have a different effect on the flow field when compared to when H_2 is the fuel, as the flame front will behave differently in this case. The failure of the model to capture the effect of pressure on NOx emissions highlights the significant effects of turbulence-chemistry interactions. As mentioned by Dutka et al. [12] changes in the flow field are likely to influence NOx formation. It highlights the need for more measurements at different flow rates for satisfactory modeling. It was however shown that at similar conditions the model predicted emissions well, showing that it is possible to use data from the non-reactive flow field to predict NOx emissions.

4.2.4 Conclusions

Since the model did not scale well at elevated pressures it was difficult to make a conclusion as to if NOx emissions are at an acceptable level when using H_2 as a fuel compared to CH_4. The model does however indicate that combustion with H_2/air results in higher NOx emissions which was expected. The model did however satisfactorily predict NOx with CH_4/air combustion, implying that the model is capable of correct predictions, however, the model struggled with predicting correct emissions from H_2/air combustion. It could be due to the fact that the difference between the non-reacting and reacting flow fields is too large when H_2 is used as fuel, and warrants further investigation.

4.3   Uncertainty analysis

The Margin of Error (MoE) was calculated for each measurement with Equation 3.1, and the mean was taken for each profile. All values are displayed in Appendix A. No mean MoE was found to be larger than 1.4% in the mean axial velocity profiles, while no mean MoE was found to be larger than 2.9% in the mean radial velocity profiles. The most significant source of uncertainty in the experiments was likely related to manual measurements. These measurements were required to determine the distance between the laser beams emitted from the laser head. This was done without the lens mounted on the laser head to ensure that the beams traveled without converging. The horizontal beams were measured manually with an uncertainty of ± 0.2 mm, while the uncertainty in the vertical beams was slightly larger, at ± 0.3 mm. These measurements were used as input data for the processor to compute mean velocities and RMS values. The precise impact of these uncertainties on the calculations is difficult to quantify. Nevertheless, it's important to acknowledge these manual measurements as a potential source of uncertainty in the experiments.

As discussed by Simmons [53], there was also uncertainty linked to the instrumentation settings chosen by the user, including signal gain, velocity span, and sensitivity. These settings were adjusted at various measurement points to optimize data rates and validation of measurements. Regions with a low concentration of seeding particles required different settings compared to regions with a high concentration. This may have introduced some variability in the data. However, it's important to note that the level of uncertainty related to these adjustments is expected to be minimal.
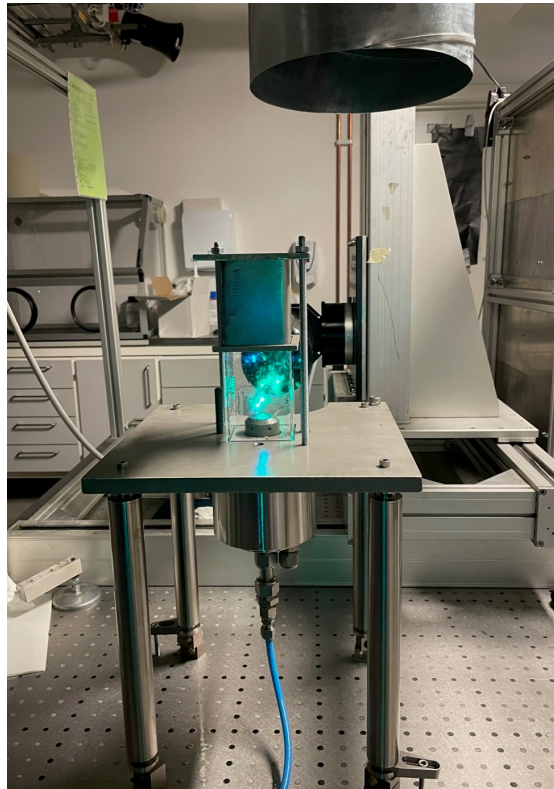
4.3.1   Sources of error

Figure 4.18: Setup displaying the offset between the chamber and the suction pipe in the top right corner of the picture.
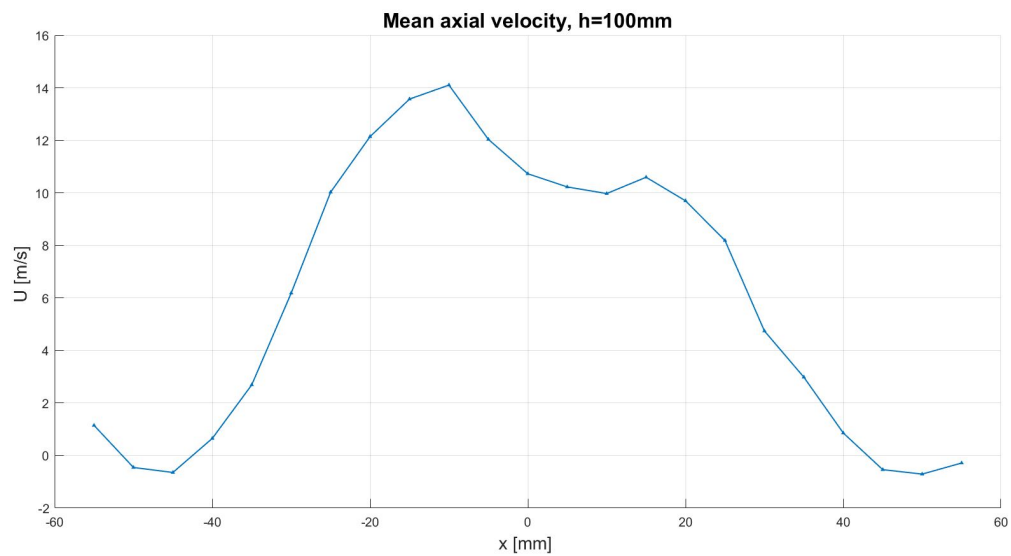

Figure 4.19: Mean axial velocity profile at $h = 100$ mm.

A possible source of error is related to the experimental setup. A suction pipe was placed above the chamber in order to dispose of any potential flue gases. The

pipe was however placed in an offset to the chamber, and at certain heights in the chamber, it seemed like this could be influencing the measurements. The offset is illustrated in Figure 4.18 and a velocity profile at $h = 100\,\text{mm}$ are shown in Figure 4.19.
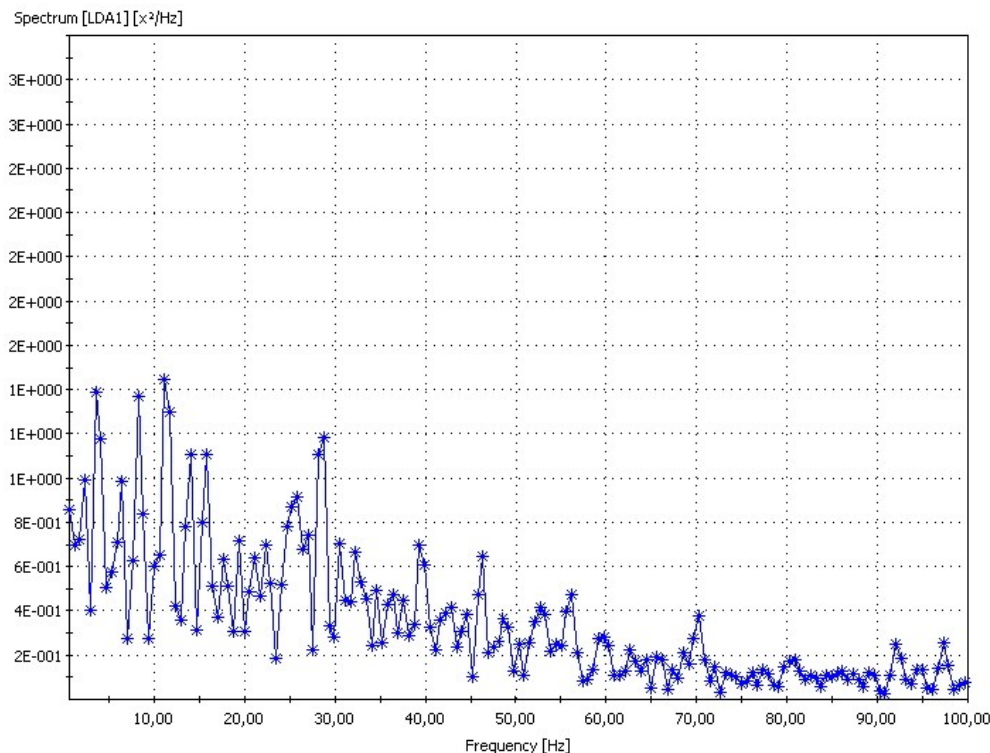
Figure 4.20: The frequency spectrum of the measured velocities at $x = -10\,\text{mm}$.

The mean velocity profile has a significant peak at $x = -10$ mm, which was not mirrored on the other side of the chamber. As the flow is 3-dimensional and asymmetrical, it was possible that it was due to a flow structure being present. If this was the case the flow could be unstable at this point and oscillate in a periodic fashion. Therefore, it was investigated if a dominating frequency was present in the data which would indicate this effect. A frequency spectrum of the measured velocities seen in Figure 4.20, shows that no peak frequency can be observed, indicating that no dominant frequency was present. It needs to be noted that the seeding rate during the experiments was not optimized for spectrum analysis, and a higher seeding rate would be needed in order to conclude with certainty. However, due to the fact that the velocity peak is located on the same side of the

chamber as the ventilation pipe was offset, it seemed likely that it has interfered with the experiments. The same effect could not be observed in the data at lower heights in the flow field, but the interference could not be excluded from them either. Due to the significant effect at $h = 100 \, \text{mm}$, the velocity profile was not considered when classifying the flow field.

Another source of error was changing conditions during the experiments. When the laser was in use for several hours, a dip in power would sometimes occur. As an effect of this fewer particles were successfully measured in the measuring volume, yielding a lower data rate. This meant that experiments conducted after the laser had been in use for an extended amount of time were of slightly lower quality than those at the start of the session. The extent of the error associated with this is hard to quantify, but it is acknowledged.

4.4 Future work

Investigation of the instantaneous flow field: As the flow field was shown to be highly 3-dimensional and complex, further investigations on the instantaneous flow field are recommended. The flow field did contain large fluctuations and high turbulence intensities. PIV measurements could give useful insights into whether instabilities in the flow field were present due to this and could reveal the presence of complex flow structures. As discussed in section 4.1.4, the determination of the volumes of the recirculation zone, PSR and PFR are based to a high degree on assumptions. A 2D velocity map from PIV measurements could help classify the size of any recirculating zones accurately.

In flame measurements: Measurements with the same operating conditions with a reacting flow would give insight into the turbulence-chemistry interactions, which are highly valuable. The expansion of the recirculating zones could be quantified, and the effect of the increased momentum due to this on the mean velocity. Furthermore, the effect of increased turbulence intensities on the formation of NOx could be investigated, which would provide valuable insight into the relationship between the turbulent flow field and chemical kinetics. Additionally, it would be

useful to perform measurements at different flow rates to quantify the effect of different turbulence levels on NOx emissions.

Model improvements: Measures could be made to improve the CRN model. Heat losses to the walls could be incorporated which effects are discussed in Section 4.2.1. Further stratification of the PSR in addition to stratification of the PFR could be made, with inlet conditions that were more representative of the flow field at the given locations, which could capture flow field effects more precisely. This would however need more detailed measurements of the flow field in order to find the correct inlet conditions at the given zones in the reactors model. Optimization of the model could also be performed through sensitivity analysis.

Experiments with different burner configurations and fuels: This investigation provided a detailed characterization of the flow field for a specific burner configuration. However, it is crucial to note that the underlying principles and the analytical approach can be applied to a broader range of burner configurations such as Partially Premixed Bluff Body burners (PPBB). By considering and investigating diverse burner arrangements, comprehensive conclusions could be drawn that surpass the limitations of a single combustion system. This cross-system analysis would provide a more robust understanding of combustion dynamics, enhancing the universality and applicability of the findings to other gas turbine configurations.

This would also be helpful in order to validate generalized numerical models. It would also be helpful to expand the analysis to other fuels since the transition from fossil fuels to low carbon emitting fuels can not only be achieved with H_2. Another promising fuel that warrants investigation is NH_3, which emits fuel-bound NOx. Its interactions with turbulence-chemistry interactions are inherently different and need research to be implemented in future combustion systems. Additionally, fuel compositions of mixed CH_4 and H_2 could help resolve some of the challenges with H_2/air combustion while simultaneously require minimal changes to existing gas turbine configurations and lower carbon emissions. This could be an intermediate step before technology for pure H_2/air combustion is in place.

CONCLUSIONS

5.1 Objective

This thesis aimed to characterize the swirling flow field above a laboratory-scale gas turbine burner. To investigate the isothermal flow field, Laser Doppler Velocimetry (LDV) measurements were applied, which enabled the classification of recirculation zones and residence times within the burner. They served as input into a Chemical Reactor Network (CRN). NOx emissions from combustion of H_2/air and CH_4/air resulting in a power output of $10\,kW$ and $T_{ad} = 1563\,K$ were simulated with the CRN, which corresponds to the mass flow rate of air at which the experiments were conducted with.

5.2 Results

One of the questions the thesis aimed to answer was if it was possible to use non-reacting velocity field data to simulate NOx emissions from a flame with a similar mass flow rate of air used in the experiments. It proved to be successful when using CH_4 as fuel, however, simulations could not reproduce measured values of NOx when H_2 was fuel. It also aimed to answer how using H_2 impacted NOx

emissions, which proved indecisive due to the reason mentioned above. However, the model indicated higher NOx emissions from H_2/air combustion as expected.

5.2.1   The swirling velocity field

The LDV measurements revealed a distinctive Outer Recirculation Zone (ORZ), with a height of $h = 40\,\mathrm{mm}$, that was identified at the left side of the combustion chamber. The onset of an Internal Recirculation Zone (IRZ) was indicated at the center of the flow field, however, the swirl was not intense enough to induce recirculation in this area. The flow field proved to be highly 3-dimensional and there were indications of possible instabilities. Given these complexities and potential instabilities, it is recommended that further investigations of the instantaneous flow field are carried out. This approach could provide valuable insights into any underlying instabilities, in addition to the recirculation zones.

5.2.2   NOx emissions

Furthermore, the CRN model made simulated the formation and consumption of species in addition to the temperature development throughout the combustion chamber. The measurements of the 2D flow field were used to estimate the size of the recirculation zone, then calculate the residence time in this. Additionally, residence times in the Perfectly Stirred Reactor (PSR) and Plug Flow Reactor (PFR) constituting the CRN were estimated. They were found to be: $\tau_{PSR} = 0.227\,\mathrm{ms}$, $\tau_{PFR} = 0.248\,\mathrm{ms}$, and $\tau_{recirc} = 0.274\,\mathrm{ms}$. The simulated values were validated against existing experimental data. Notably, the model demonstrated a satisfactory prediction of NOx emissions under conditions similar to those used in the experiments for CH_4 as fuel with an absolute error of $3\,\mathrm{ppm}$.

With H_2 as fuel, the simulated values were satisfactory at a slightly higher flow rate than the one used in experiments, however, it could not predict accurately the emissions at the same conditions. The simulated value, in this case, exhibited an overestimation of $9\,\mathrm{ppm}$. To enhance the model's accuracy and resilience to varied conditions, it is recommended that additional measurements of the flow field are conducted. These tests should be conducted under varying conditions, encompass-

ing both reacting and non-reacting flows. The results would serve two primary purposes: further validating the model and providing a deeper understanding of the turbulence-chemistry interactions.

The findings of this thesis have yielded valuable insights into the nature of the turbulent flow field above the swirl-stabilized burner. Moreover, the data collected can be employed as a reference database for validating future numerical models. It also yields insight into the possibility to utilize H_2 as a fuel in gas turbine applications.

REFERENCES

[1] Norsk Petroleum. "EMISSIONS TO AIR". In: (2022). URL: `https://www.norskpetroleum.no/en/environment-and-technology/emissions-to-air/`.

[2] General Electric. "Decarbonizing gas turbines through carbon capture". In: (2022). URL: `https://www.ge.com/content/dam/gepower-new/global/en_US/downloads/gas-new-site/future-of-energy/decarbonizing-gas-turbines-ccus-gea34966.pdf`.

[3] Various. *NOx*. 2022. URL: `https://en.wikipedia.org/wiki/NOx#Health_and_environment_effects`.

[4] Agency for toxic substances and disease registry. "NITROGEN OXIDES". In: (2002). URL: `https://www.atsdr.cdc.gov/toxfaqs/tfacts175.pdf`.

[5] Redaksjonen Gemini. *Why is there such a fuss about NOx?* 2016. URL: `https://norwegianscitechnews.com/2016/05/hva-er-det-egentlig-med-denne-nox-en/`.

[6] W. Meier, X.R. Duan, and P. Weigand. "Investigations of swirl flames in a gas turbine model combustor: II. Turbulence–chemistry interactions". In: *Combustion and Flame* 144 (2006), pp. 225–236. DOI: `https://doi.org/10.1016/j.combustflame.2005.07.009`.

[7] Aleksei S. Lobasov et al. "Mass and momentum transport in the near field of swirling turbulent jets. Effect of swirl rate". In: *International Journal of Heat and Fluid Flow* 83 (2020), pp. 108–539. DOI: `https://doi.org/10.1016/j.ijheatfluidflow.2020.108539`.

[8] Fabio Cozzi, Aldo Coghe, and Rohit Sharma. "Analysis of local entrainment rate in the initial region of isothermal free swirling jets by Stereo PIV". In: *Experimental Thermal and Fluid Science* 94 (2018), pp. 281–294. DOI: https://doi.org/10.1016/j.expthermflusci.2018.01.013.

[9] P. Schmittel et al. "Turbulent swirling flames: Experimental investigation of the flow field and formation of nitrogen oxide". In: *Proceedings of the Combustion Institute* 28 (2000), pp. 303–309. DOI: https://doi.org/10.1016/S0082-0784(00)80224-6.

[10] Aldo Coghe, Giulio Solero, and Gianfranco Scribano. "Recirculation phenomena in a natural gas swirl combustor". In: *Experimental Thermal and Fluid Science* 28 (2004), pp. 709–714. DOI: https://doi.org/10.1016/j.expthermflusci.2003.12.007.

[11] N. Syred, N.A. Chigier, and J.M. Beér. "Flame stabilization in recirculation zones of jets with swirl". In: *Symposium (International) on Combustion* 13 (1971), pp. 617–624. DOI: https://doi.org/10.1016/S0082-0784(71)80063-2.

[12] Marcin Dutka, Mario Ditaranto, and Terese Løvås. "NOx emissions and turbulent flow field in a partially premixed bluff body burner with CH4 and H2 fuels". In: *International Journal of Hydrogen Energy* 41 (2016). DOI: https://doi.org/10.1016/j.ijhydene.2016.05.154.

[13] P. Weigand et al. "Investigations of swirl flames in a gas turbine model combustor: I. Flow field, structures, temperature, and species distributions". In: *Combustion and Flame* 144 (2006), pp. 205–224. DOI: https://doi.org/10.1016/j.combustflame.2005.07.010.

[14] T. Capurso et al. "NOx pathways in lean partially premixed swirling H2-air turbulent flame". In: *Combustion and Flame* 248 (2023), p. 112581. DOI: https://doi.org/10.1016/j.combustflame.2022.112581.

[15] Martin Skottene and Kjell Erik Rian. "A study of NOx formation in hydrogen flames". In: *International Journal of Hydrogen Energy* 32 (2007). DOI: https://doi.org/10.1016/j.ijhydene.2007.02.038.

[16] Peter Glarborg et al. "Modeling nitrogen chemistry in combustion". In: *Progress in Energy and Combustion Science* 67 (2018), pp. 31–68. DOI: `https://doi.org/10.1016/j.pecs.2018.01.002`.

[17] Ekenechukwu Chijioke Okafor et al. "Measurement and modelling of the laminar burning velocity of methane-ammonia-air flames at high pressures using a reduced reaction mechanism". In: *Combustion and Flame* 204 (2019), pp. 162–175. DOI: `https://doi.org/10.1016/j.combustflame.2019.03.008`.

[18] Sindre Ertzgaard Solvang. "A Numerical Simulation of Combustion with Ammonia/Methane Fuel Blends: Investigating the Impact on NOx Emissions". In: (2023).

[19] Stephen R. Turns. *AN INTRODUCTION TO COMBUSTION. Concepts and Applications.* 3rd edition. McGraw-Hill, 2012.

[20] Bj¨orn Baumgarten. "Residence Time Distribution". In: (2021). URL: `https://folk.ntnu.no/preisig/HAP_Specials/Felles_lab/Experiments/RE9_milli-reactor_residence_time.pdf`.

[21] E. Bruce Nauman. "Residence Time Theory". In: *Industrial & Engineering Chemistry Research* 47 (2008). DOI: `10.1021/ie071635a`.

[22] Rodney O. Fox. *Computational Models for Turbulent Reacting Flows.* Cambridge University Press, 2003.

[23] United States Office of Air Quality. *Nitrogen Oxides (NOx), Why and How They are Controlled.* 1999. URL: `https://www3.epa.gov/ttncatc1/dir1/fnoxdoc.pdf`.

[24] Wai Siong Chai et al. "A review on ammonia, ammonia-hydrogen and ammonia-methane fuels". In: *Renewable and Sustainable Energy Reviews* 147 (2021), pp. 111–254. DOI: `https://doi.org/10.1016/j.rser.2021.111254`.

[25] Klaus G. Moesl. *The NOx Formation Routess.* 2012. URL: `https://link.springer.com/content/pdf/10.1007/978-3-030-51166-1_2.pdf`.

[26] M. Khosravy el Hossaini. "Review of the New Combustion Technologies in Modern Gas Turbines". In: (2012). URL: `https://www.intechopen.com/chapters/45115`.

[27] Yasir M. Al-Abdeli and Assaad R. Masri. "Review of laboratory swirl burners and experiments for model validation". In: *Experimental Thermal and Fluid Science* 69 (2015), pp. 178–196. DOI: `https://doi.org/10.1016/j.expthermflusci.2015.07.023`.

[28] Toufik Boushaki. "Introductory Chapter: Swirling Flows and Flames". In: (2015). URL: `https://www.intechopen.com/chapters/67203`.

[29] Paul O. Hedman et al. "Observations of Flame Behavior in a Laboratory-Scale Pre-Mixed Natural Gas/Air Gas Turbine Combustor From PLIF Measurements of OH". In: *Paper GT2002-30052, ASME Turbo Expo 2002: Power for Land, Sea, and Air* (2009).

[30] Ruigang Zhou. "Swirl Number for Non-Reacting and Reacting conditions of Cambridge Stratified Swirl Burner". In: (2018). URL: `https://www.repository.cam.ac.uk/bitstream/handle/1810/243259/DSpace_velocity_SwirlNumber_CSB_LDA.pdf;sequence=4`.

[31] S. Terhaar et al. "Suppression and excitation of the precessing vortex core by acoustic velocity fluctuations: An experimental and analytical study". In: *Combustion and Flame* 172 (2016), pp. 234–251. DOI: `https://doi.org/10.1016/j.combustflame.2016.06.013`.

[32] Reza Rezvani. *A CONCEPTUAL METHODOLOGY FOR THE PREDICTION OF ENGINE EMISSIONS*. 2010. URL: `https://smartech.gatech.edu/bitstream/handle/1853/42932/rezvani_reza_201012_phd.pdf?%20sequence=1&isAllowed=y`.

[33] Stephen B. Pope. *TURBULENT FLOWS*. Cambridge University Press, 2013.

[34] MIT. *Basics of Turbulent Flow*. URL: `https://www.mit.edu/course/1/1.061/www/dream/SEVEN/SEVENTHEORY.PDF`.

[35] Ivar Ståle Ertesvåg. *TURBULENT STRØYMING OG FORBRENNING. Frå turbulensteori til ingeniørverktøy*. Tapir akademisk forlag, 2000.

[36] Cheng Tung Chong and Jo-Han Ng. "Chapter 4 - Combustion performance of biojet fuels". In: *Biojet Fuel in Aviation Applications*. Ed. by Cheng Tung Chong and Jo-Han Ng. Elsevier, 2021, pp. 175–230. DOI: `https://doi.org/10.1016/B978-0-12-822854-8.00002-0`.

[37]   *Laminar burning velocity and laminar flame thickness.* 2009. URL: `http://www.hysafe.net/wiki/BRHS/LaminarBurningVelocityAndLaminarFlameThickness`.

[38]   Poinsot T. and Veynante D. *Theoretical and numerical combustion.* Philadelphia: Edwards, 2001.

[39]   *Borghi-diagram and interpretation of combustion regimes.* 2008. URL: `http://www.hysafe.net/wiki/BRHS/Borghi-diagramAndInterpretationOfCombustionRegim`

[40]   K. Dobrego and A. Chorny. "Parallels between the Regimes of Turbulent and Filtration Combustion of Gases in Inert Porous Media". In: *Journal of Engineering Physics and Thermophysics* 74 (2001), pp. 581–590. DOI: `10.1023/A:1016791807624`.

[41]   *Premixed flame.* 2023. URL: `https://en.wikipedia.org/wiki/Premixed_flame`.

[42]   *Non-premixed Turbulent Combustion.* 2007. URL: `https://www.osti.gov/servlets/purl/1714512`.

[43]   *Thermal Properties of Fused Quartz.* 2018. URL: `https://www.qsiquartz.com/thermal-properties-fused-quartz/`.

[44]   M. Ditaranto et al. "EXPERIMENTAL AND NUMERICAL RESULTS OF A NON-DLE AERODERIVATIVE GT COMBUSTION SYSTEM BURNING METHANE-AMMONIA BLENDS AT INTERMEDIATE PRESSURES". In: *Paper GT2023-103074, ASME Turbo Expo 2023 Turbomachinery Technical Conference and Exposition, Boston Massachutes USA (Submitted)* (3-26-2023).

[45]   Dantec Dynamics. "Measurement Principles of LDA". In: (2022). URL: `https://www.dantecdynamics.com/solutions/fluid-mechanics/laser-doppler-anemometry-lda/measurement-principles-of-lda/`.

[46]   DANTEC. *BSA Flow Software. Installation User's guide.* 2000.

[47]   Emerson Process Management. *Brooks Microprocessor Control Read Out Unit Models 0152/0154.* English.

[48]   Majid Bahrami. "Integral Relations for CV". In: (2009). URL: `https://www.sfu.ca/~mbahrami/ENSC%5C%20283/Notes/Integral%5C%20Relations%5C%20for%5C%20CV_Part%5C%201.pdf`.

[49]   PyData. *Cantera.* 2022. URL: `https://pydata.org/project/cantera/`.

[50] Cantera Developers. *Reactor models in Cantera*. 2022. URL: https://cantera.
      org/science/reactors/reactors.html.

[51] Cantera. "Zero-Dimensional Reactor Networks". In: (2021). URL: https://
      cantera.org/documentation/docs-2.5/sphinx/html/cython/zerodim.
      html.

[52] Mario Ditaranto. "Unpublished data, LowEmission Center SP6 Case Study
      Eglin-Franklin oil fields". 2021.

[53] Daniel Simmons. "Laser Doppler Velocimetry (LDV) Measurements". In:
      (2020). URL: https://turbmodels.larc.nasa.gov/Other_exp_Data/
      Notredame_sep/Documentation/LDV-Documentation.pdf.

APPENDICES

A - MARGIN OF ERROR

The tables presented in Appendix A provide the associated Margins of Error of the measured velocity profiles. These tables serve as a reference for the data uncertainty analysis discussed in Section 4.3.

Table A.1: Mean MoE for profiles along the y-axis at $h = 60$ mm.

Y profile	Mean MoE axial velocity	Mean MoE radial velocity
x=-20 mm	0.39	1.41
x=-15 mm	0.34	0.94
x=-10 mm	0.86	1.95
x=-5 mm	0.45	0.66
x= 0 mm	0.93	1.07
x=5 mm	0.44	0.85
x=10 mm	0.52	1.07
x= 15 mm	0.57	2.3
x= 20 mm	0.41	2.83

Table A.2: MoE for profiles along y-axis at $h = 30$ mm.

Y profile	Mean MoE axial velocity	Mean MoE radial velocity
x=-20 mm	1.22	0.49
x=-15 mm	1.11	0.52
x=-10 mm	1.18	0.57
x=-5 mm	0.82	0.69
x= 0 mm	0.38	0.89
x=5 mm	1.05	0.43
x=10 mm	1.14	0.52
x= 15 mm	0.73	0.47
x= 20 mm	1.06	0.43

Table A.3: Mean MoE of mean axial and radial velocity for profiles along the x-axis at $h = 30$ mm and $h = 60$ mm.

Y profiles, $h = 60$ mm	MoE mean axial velocity	MoE mean radial velocity
y=-20 mm	0.26	1.34
y= -10 mm	0.73	1.08
y=10 mm	0.72	1.25
y=20 mm	0.28	1.86
Y profiles, $h = 30$ mm		
y=-20 mm	0.73	0.53
y=-10 mm	1.31	0.57
y=10 mm	1.0	0.54
y=20 mm	0.58	0.61

Table A.4: Mean MoE for profiles along the x-axis. All measurements are conducted at y= 0mm.

Height above burner tip [mm]	Mean MoE mean axial velocity [%]	Mean MoE mean radial velocity [%]
15	0.504	0.36
30	0.92	1.0
40	0.73	1.01
60	0.50	0.86
85	1.07	0.33